Marine Geology 450 (2022) 106842

Contents lists available at ScienceDirect

Marine Geology

journal homepage: www.elsevier.com/locate/margo

Research Article

Coastal palaeoenvironmental record of Late Bronze to Iron Age harbour development at Liman Tepe-Clazomenae, western Anatolia, Turkey

Nicholas L. Riddick [a,*], Joseph I. Boyce [a,*], Vasıf Şahoğlu [b], Hayat Erkanal [b], İrfan Tuğcu [c], Yeşim Alkan [c], Eduard G. Reinhardt [a], Beverly N. Goodman-Tchernov [d]

[a] School of Earth, Environment and Society, McMaster University, Hamilton, Canada
[b] Department of Archaeology Ankara University, Ankara University Mustafa V. Koç Research Center for Maritime Archaeology (ANKÜSAM), Izmir, Turkey
[c] Department of Archaeology, Osmaniye Korkut Ata University, Osmaniye, Turkey
[d] Department of Marine Geosciences, Haifa University, Haifa, Israel

ARTICLE INFO

Editor: Edward Anthony

Keywords:
Liman Tepe-Clazomenae
Archaic harbour
Late Bronze-early Iron Age transition
Proto-harbour
Palaeoenvironments
micro-XRF core scanning
Lithochemofacies
Geophysical surveys

ABSTRACT

Liman Tepe-Clazomenae, located in the southern Bay of Izmir, Turkey, was an important Early Bronze Age to Classical Period trading port and cultural centre in the eastern Aegean. The mainland harbour, now submerged ~1.5–2 m below present sea level, is one of the best-preserved examples of an Iron Age (Archaic Period; ca. 7th–6th c. BCE) semi-enclosed harbour (>5 ha) with engineered breakwater structures. A multi-proxy study (micropalaeontology, micro-XRF core scanning) was conducted on seven harbour sediment cores and integrated with geophysical data to map the harbour structures and document coastal palaeoenvironmental changes. Bathymetry and side-scan mapping revealed two broad (>35 m) rubble-constructed breakwater structures and a submerged headland that divided the harbour into two separate sub-basins. Linear magnetic anomalies within the eastern breakwater indicate a buried pier structure, recording possible augmentation of a Late Bronze Age (LBA) or Early Iron Age (EIA) proto-harbour embayment. The harbour basin stratigraphy comprises foreshore and upper shoreface deposits overlying terrigenous clays across a marine transgressive surface. A distinctive silt-rich chemofacies with increased Ti/Ca and decreased Si marks a transition from a sandy marine shoreface to a low energy, sheltered LBA proto-harbour embayment. The Iron Age harbour construction (ca. 7th–6th c. BCE) is recorded by a rise in *Rosalina*, decreased Ti/Ca and the appearance of Archaic pottery. The harbour was in use from the Archaic to early Classical periods and served as Clazomenae's mainland commercial port.

1. Introduction

The Iron Age (ca. 1200–114 BCE) was a period of major cultural change and technological development in the Aegean (Dickinson, 2006; Papadopoulos, 2014). An important innovation was the introduction of semi-enclosed artificial harbour basins with engineered harbour structures (e.g., breakwaters, piers, quays) (Mauro, 2019; Mauro and Gambash, 2020). During the Bronze Age (ca. 3000–1200 BCE) naturally sheltered lagoons, river mouths and coastal embayments formed in the lee of headlands were utilized as anchorage sites (Marriner et al., 2005, 2014; Tartaron, 2013; Mauro, 2019). In the Iron Age, natural 'proto-harbour' embayments were augmented with engineered structures to allow harbouring under a range of weather conditions and sea states (Marriner et al., 2014; Shalev et al., 2019). In the Aegean, the transition from natural to semi-artificial, engineered harbours began during the Early Iron Age (EIA), with the earliest evidence for man-made breakwater structures dating to the 8th–7th c. BCE at Delos (Flemming, 1980; Duchêne and Fraisse, 2001). By the late 6th to early 5th c. BCE, harbour breakwaters were constructed as extensions of city fortification walls (Mauro, 2019; Mauro and Gambash, 2020).

On the Levant coast of the eastern Mediterranean, the augmentation of natural harbour basins with protective structures began earlier, perhaps as early as the Middle Bronze Age (MBA) to Late Bronze Age (LBA) (Raban, 1995; Tartaron, 2013). Raban (1995) described ashlar-constructed quays at Dor (Israel) that were built in the LBA and modified during the EIA. Ashlar quays were employed in the construction of the Phoenician harbour at Atlit (Israel) between the 9th–7th c. BCE (Haggi, 2006; Haggi and Artzy, 2007). At Sidon (Lebanon), nearshore sandstone ridges were augmented with rubble constructions to protect natural embayments during the MBA to LBA (Marriner et al., 2006) and

* Corresponding authors.
E-mail addresses: nriddick@brocku.ca (N.L. Riddick), boycej@mcmaster.ca (J.I. Boyce).

https://doi.org/10.1016/j.margeo.2022.106842
Received 28 October 2021; Received in revised form 25 May 2022; Accepted 30 May 2022
Available online 1 June 2022

at Tel Hreiz (Israel), rubble-constructed seawalls were in use during the Neolithic (Galili et al., 2019). In the Aegean, in contrast, there are no well-documented examples of pre-Iron Age man-made harbour structures and the LBA-EIA transition from natural proto-harbours to engineered harbour basins is not well understood (Tartaron, 2013; Mauro, 2019).

In this paper, we report on detailed geoarchaeological and geophysical investigations of a well-preserved Iron Age (Archaic Period, ca. 7th–6th c. BCE) harbour basin at Liman Tepe-Clazomenae, in western Turkey (Fig. 1). The Archaic harbour basin (>5 ha) was enclosed by two broad (>35 m wide) rubble-constructed breakwater structures, which are now submerged ~1.5–2 m below present sea level (Erkanal, 2014a). Clazomenae's Archaic harbour is one of the best-preserved in the Aegean, but its date of construction, layout, and function were not well understood. A multi-proxy study was conducted on seven marine sediment cores from the harbour basin (Fig. 1a) to document changes in the coastal palaeoenvironments stemming from harbour development and LBA-EIA land use changes. Core data were combined with geophysical mapping (bathymetry, side-scan sonar, magnetic surveys) to better resolve the harbour layout and construction. Micro-XRF core scanning (μ-XRF-CS) and chemofacies analysis (Craigie, 2018) were employed to identify the onset of harbour development and to investigate the record of anthropogenic land-use changes in harbour sediments. The results provide important insights into harbouring activities at Liman Tepe-Clazomenae, from a LBA proto-harbour phase (ca. 1600–1200 BCE) to the construction of the engineered Iron Age harbour basin in the 7th–6th c. BCE.

2. Study area

2.1. Physical setting and geology

Liman Tepe-Clazomenae is located on the south shore of the Bay of Izmir, near Urla, in western Turkey (Fig. 1). The Bay of Izmir is 64 km-long, west-east embayment of the Aegean Sea with a maximum water depth of about 100 m (Fig. 1b) (Sayın, 2003). The bay is microtidal (~20–50 cm) and the primary sediment input is from the Gediz River (Fig. 1b). In the eastern sector of the bay, currents are dominantly clockwise, transporting sediment eastward from the Gediz estuary and then westward along the south shore towards Urla (Sayın and Eronat, 2018) (Fig. 1b). The westward longshore sediment transport has caused progradation of beaches to the east of Karantina Island and was accelerated by the construction of a causeway linking the mainland with the island in the 4th c. BCE by the forces of Alexander the Great (Goodman et al., 2008; Krezoski, 2008) (Figs. 1a, 2a).

The bedrock in the Urla region consists of Neogene carbonate and clastic sedimentary rocks interbedded with middle Miocene volcanics (Kaya, 1979; Göktaş, 2016). The Liman Tepe headland is formed from

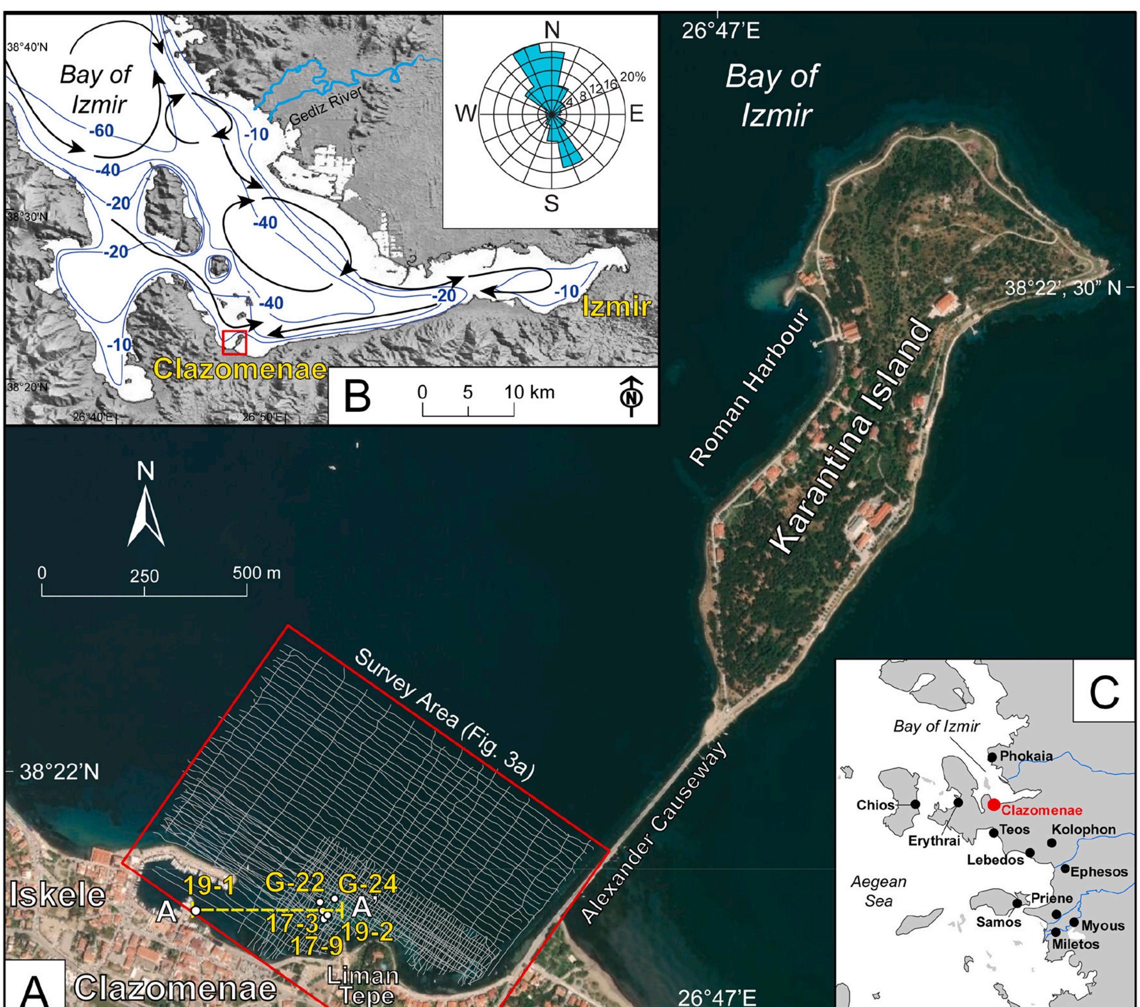

Fig. 1. A. Satellite image of Liman Tepe-Clazomenae study area showing geophysical survey tracklines and coring transect (A-A'). B. Generalized bathymetric map of Bay of Izmir showing study area location, wind directions (inset) and water circulation patterns (after Sayın, 2003). C. Location of Clazomenae and other Ionian League cities in western Anatolia, Turkey.

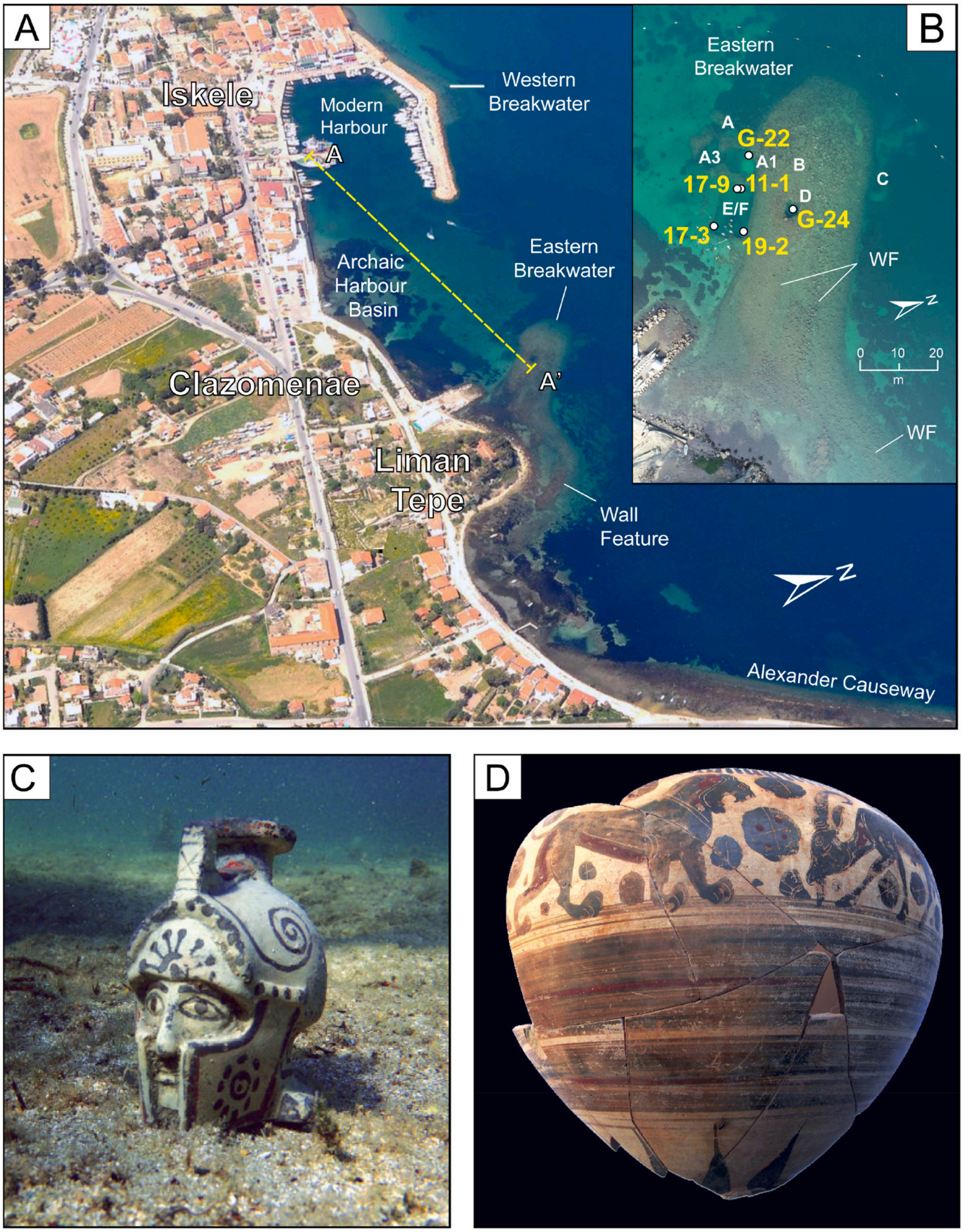

Fig. 2. A. Aerial photo showing submerged Archaic (ca. 7th c. BCE) breakwater structures in Clazomenae's mainland harbour basin and location of core transect A-A' (Fig. 7) (photo: Hakan Çetinkaya). B. Aerial image of eastern breakwater showing excavation areas (A-F),core locations and wall features (WF) on mole surface. C. Archaic Period (ca. 7th–6th c. BCE) ceramic perfume bottle, fashioned in the shape of warrior's head. D. Archaic Period 'Wild Goat' style vessel.

Neogene limestone and mudstone and to the west, bedrock is composed dominantly of volcanic (trachyte-andesite) extrusive rocks (Kayan et al., 2019). Bedrock is overlain by a variable thickness of unconsolidated, Quaternary and Holocene alluvial and coastal plain sediments. To the west of Karantina Island, surficial sediments are between 1 and 20 m thick and volcanic bedrock is exposed at surface in highland areas to the south and west of the site (Kayan et al., 2019; Riddick et al., 2022a).

2.2. Site history and archaeology

Ancient Clazomenae occupied the mainland areas of the coast around the modern port town of Iskele and Karantina Island (Fig. 1a). The city was founded by Ionian and Greek settlers in the 11th–9th c. BCE and was an important Iron Age olive-producing centre and trading port (Aytaçlar, 2004; Ersoy, 2004). Clazomenae was founded on top of the prehistoric (Chalcolithic-Bronze Age) settlement of Liman Tepe, which was located on the coastal headland east of the town of Iskele (Figs. 1a, 2a). Liman Tepe was an important Early Bronze Age (EBA) trade centre in the Anatolian Trade Network (Erkanal, 2008; Şahoğlu, 2005). In the 6th–5th c. BCE, Clazomenae's citadel was moved from the mainland to Karantina Island (Fig. 1b), due to conflict with the Persians (Ersoy, 2004).

Underwater excavations at Liman Tepe-Clazomenae have been ongoing since 2005, focusing on the eastern Archaic harbour basin (Fig. 2b) (Erkanal, 2014a). Recent work has yielded a wealth of pottery and other cultural materials (Figs. 2c, d) that indicate intensive use of the harbour as a trading port in 7th–6th c. BCE (Archaic Period) and again in the 4th c. BCE (Classical Period) (Şahoğlu, 2010; Erkanal, 2014a; Tuğcu, 2017). The pottery finds include *amphorae* and *oinochoai* with distinctive 'Wild Goat style' motifs that date to the early to middle 6th c. BCE (Erkanal et al., 2014) (Fig. 2d). Coring of the eastern breakwater in Area D (Fig. 2b) recorded >5 m of collapsed masonry and coarse rubble overlying shoreface silt and mud containing seagrass (*Posidonia oceanica* L. Delile) matte layers (Goodman, 2006). Excavations in Trench A3 (Fig. 2b) uncovered the remains of an Archaic (ca. late 7th to early 6th c. BCE) wooden anchor arm embedded in harbour mud (~ 5 m bsl) (Votruba and Artzy, 2016). Investigations of the western harbour breakwater (Fig. 2a) have been limited to diver reconnaissance and test trenching in the modern harbour.

Land excavations at Liman Tepe have yielded a broad range of EBA to LBA cultural materials, including Cycladic, Minoan and Mycenean pottery, indicating a diverse maritime trade network and cultural connections that spanned the Aegean (Erkanal, 2008; Şahoğlu, 2010; Erkanal, 2014b). The earliest settlement layers date to the Middle Chalcolithic (ca. 4600 BCE) (Tuncel and Şahoğlu, 2018) and there is scattered pottery evidence for possible Neolithic occupations (Erkanal, 2008). Liman Tepe's importance as a maritime trading port would have required the availability of anchorage sites, but to date harbouring areas have not been identified. Natural coastal embayments and lagoons to the east and west of the headland may have provided sheltered mooring areas during the Bronze Age settlement phases (Goodman et al., 2009; Riddick et al., 2022a).

3. Methods

3.1. Geophysical surveys

Marine geophysical surveys were conducted over a 0.35 km^2 inshore area, including the Archaic harbour (Fig. 1a). Bathymetry and side-scan sonar swaths were collected using a 200 kHz echosounder system with 5–20 m line separations and 0.01 m inline sampling (Fig. 1a). Sonar data were corrected for tides and sensor heave and side-scan images processed and mosaiced using methods outlined by Sonnenburg and Boyce (2008). Magnetic surveys were acquired over the eastern breakwater using a towed Overhauser magnetometer with 3–5 m line separation and a 4 Hz sample rate (Fig. 1a). A base station magnetometer was deployed onshore to record diurnal magnetic variations. Magnetic data processing included diurnal corrections, tie-line leveling, and gridding of corrected magnetic data using minimum curvature algorithm with 1-m grid cells (Boyce et al., 2004).

3.2. Coring and geochemical analysis

Five cores (~1.1–3.2 m length) were collected in the Archaic harbour basin using a diver-operated percussion coring system with 70 mm diameter core tubes (Fig. 1a) (Riddick et al., 2022a). Core sedimentary lithofacies were logged in detail and elemental abundances measured on split cores using an Itrax micro-XRF core scanner (Cox Analytical Systems). Cores were scanned at 0.5 mm intervals using a 3-kW molybdenum (Mo) tube, 20 s analysis time and 30 kV/25 mA power settings. Element peak areas were normalized to the coherent/incoherent backscatter ratio (CIR) to minimize matrix effects (Kylander et al., 2011; Marshall et al., 2011; Gregory et al., 2019; Löwemark et al., 2019) and smoothed using a 5-point running average. Elemental data were combined with sedimentary facies to identify distinctive lithochemofacies within the harbour basin stratigraphy (Ramkumar, 2015; Craigie, 2018). From the available elements, Si, and Ti were selected as indicators of terrigenous sediment input, and Ca and Br as indicators of marine biogenic productivity. Ca is commonly used as an indicator of $CaCO_3$ (aragonite) production and Br as an indicator of marine plant organic matter content (Rothwell and Croudace, 2015; Ziegler et al., 2008; Seki et al., 2019). The Ti/Ca ratio was used to determine variations in terrestrial sediment input relative to biogenic $CaCO_3$ production, and as a tool for core correlation (Piva et al., 2008; Koster et al., 2015; Pint et al., 2015; Riddick et al., 2022a). The covariances in selected elemental abundances were evaluated using Pearson correlation in the R package *Corrplot* (Wei et al., 2017).

3.3. Micropalaeontology and core chronology

Micropalaeontological analysis (foraminifera) was completed on two cores (17–9, 19–1) (Fig. 1a). 2.5 cc sediment samples were divided into eight aliquots using a wet splitter (Scott and Hermelin, 1993) and ~ 100 individual foraminifera counted in each sub-sample and identified to the *genus* level with reference to previous work (Krezoski, 2008; Goodman et al., 2009). Palaeoenvironmental interpretations were aided by comparison with lithofacies and foraminifera biofacies from two cores (G-22 and G-24; Fig. 2b) from Goodman (2006).

AMS ^{14}C dates were obtained on 15 organic samples, including marine shells, seaweed (*P. oceanica*), terrestrial bulk organics and seeds (A.E. Lalonde Laboratory, Ottawa; Direct AMS, Washington, USA) (Table 1). ^{14}C ages were calibrated in Calib 8.2 (Stuiver et al., 2021) using the IntCal20 and Marine20 calibration curves (Reimer et al., 2020; Heaton et al., 2020). The marine reservoir effect (MRE) was corrected initially using a mean ΔR value of −35 ± 60, estimated from three Aegean sites in the Calib 8.2 online database (Reimer and Reimer, 2001; Stuiver et al., 2021). The regional ΔR correction, however, produced calibrated ages that were > 400 years younger than the established archaeological chronology, which indicated a 7th–6th c. BCE age for the basal harbour sediments (Erkanal, 2014a; Erkanal et al., 2014; Votruba and Artzy, 2016). To resolve this, a local ΔR value was determined using two AMS ^{14}C dates on paired (contemporaneous) terrestrial and marine organic samples (olive pit and *P. oceanica* seagrass) from 4.75 m depth in core 11–1 (Table 1) using the online *deltar* application (Reimer and Reimer, 2017). The local correction value ($\Delta R = -193 \pm 81$) indicates a significant negative offset in the local MRE relative to the regional estimate for the Aegean, which we interpret as proximity to a river mouth and mixing of riverine and marine waters (Ascough et al., 2004; Alves et al., 2018). The local ΔR correction was applied to all marine samples and produced calibrated ages that were consistent with the established archaeological chronology (Table 1).

A Bayesian age-depth model was constructed using 8 calibrated marine AMS ^{14}C dates from cores 17–9 and 11–1 in the R-package *rbacon* (Blaauw and Christen, 2011). The age of the sediment surface in the age-depth model (4.6 m depth) was assigned to the early 6th c. BCE based on pottery ages. The core chronology was also determined by 8 additional AMS ^{14}C dates in cores 19–1, 19–2, G-22, G-24 (Table 1).

4. Results and interpretation

4.1. Geophysics

4.1.1. Bathymetry and side-scan sonar

The bathymetry and side-scan sonar mapping delineated two submerged breakwater structures at depths of 1–3 mbsl in the eastern and western harbour (Fig. 3). The breakwaters enclose an extensive, semi-enclosed harbour basin (>5 ha), which was divided into two separate sub-basins by a submerged bedrock promontory (Figs. 3, 4). The eastern breakwater is approximately 120 m in length and 35 m wide with a

Table 1
AMS ^{14}C radiocarbon dates. All dates calibrated using Calib 8.2 (Stuiver et al., 2020) with the IntCal20 and Marine20 calibration curves (Reimer et al., 2020; Heaton et al., 2020). Dates from Goodman (2006; G-22, G-24) also re-calibrated. *Marine reservoir correction applied using $\Delta R = -193 \pm 81$ determined on paired (contemporaneous) marine and terrestrial samples from core 11–1 (4.75 m) (Reimer and Reimer, 2017). ** Suess Effect. The errors on ^{14}C ages (1σ) are based on counting statistics and $^{14}C/^{12}C$ and $^{13}C/^{12}C$ variation between data blocks (Crann et al., 2017).

Lab Code	Core #	Material	Elevation (mbsl)	^{14}C Age (BP)	Cal. Age BCE/CE (2σ)	Median Probability BCE/CE
Beta-191880	G-22	Gastropod shell (*Bittium* spp.)*	7.60	6280 ± 40	5048–4531 BCE	4792 BCE
Beta-164096	G-24	Seagrass (*P. oceanica*)*	5.8	2710 ± 30	789–310 BCE	546 BCE
UOC-7342	17–9	Seagrass (*P. oceanica*)*	5.13	2960 ± 22	1098–588 BCE	845 BCE
UOC-9339	17–9	Seagrass (*P. oceanica*)*	5.51	3550 ± 25	1816–1308 BCE	1557 BCE
UOC-9340	17–9	Seagrass (*P. oceanica*)*	5.93	3966 ± 25	2378–1823 BCE	2091 BCE
UOC-7343	17–9	Seagrass (*P. oceanica*)*	6.22	4535 ± 22	3095–2556 BCE	2825 BCE
UOC-9341	17–9	Seagrass (*P. oceanica*)*	6.36	4682 ± 25	3312–2778 BCE	3023 BCE
UOC-7344	17–9	Seagrass (*P. oceanica*)*	6.50	4996 ± 22	3630–3142 BCE	3408 BCE
UOC-12078	19–1	Seagrass (*P. oceanica*)*	5.13	1330 ± 22	825–1255 CE	1042 CE
UOC-12824	19–1	Seagrass (*P. oceanica*)*	5.97	3445 ± 27	1684–1181 BCE	1429 BCE
UOC-12103	19–1	Bivalve shell (*Parvicardium* spp).*	6.47	6335 ± 25	5113–4605 BCE	4885 BCE
UOC-12825	19–1	Bulk sediment sample	6.91	7310 ± 43	6238–6070 BCE	6156 BCE
UOC-12220	19–1	Bulk sediment sample	6.98	7968 ± 35	7042–6747 BCE	6895 BCE
UOC-12079	19–2	Seagrass (*P. oceanica*)*	6.96	6197 ± 29	4940–4449 BCE	4695 BCE
D-AMS-045768	11–1	Seagrass (*P. oceanica*)*	4.75	2805 ± 23	869–396 BCE	649 BCE
D-AMS-045769	11–1	Olive seed (*Olea* sp.)	4.75	2500 ± 23	652–544 BCE	634 BCE
D-AMS-045770	11–1	Seagrass (*P. oceanica*)*	5.24	3363 ± 23	1568–1067 BCE	1328 BCE

surface composed of cobble- to boulder-sized rubble (Figs. 4b, 5a). The western breakwater is a broad (>50 m), >150-m-long arcuate mole structure with a similar rubble construction but is partially obscured by modern harbour structures (Figs. 3, 4a). Linear structures indicating the remains of architectural features (i.e. wall structures) were identified on the breakwater surfaces (Figs. 4a, b). A broad (>5 m wide) arcuate wall feature, composed of coarse rubble, extends eastward from the eastern breakwater and encircles the base of the Liman Tepe headland (Figs. 4b, 5a). The wall feature may represent a possible fortification wall or seawall barrier. A narrow 20-m long, 'prong-like' projection on the northwest tip of the eastern breakwater indicates a quay or pier structure, which encloses a small basin (Figs. 4b, 5a). The recurved form of the western breakwater indicates that a sheltered harbour basin existed to the south in the area now occupied by the modern breakwater (Fig. 4a). Side-scan imaging identified several rectilinear features indicating the remains of architectural features on the submerged headland dividing the two harbour basins (Figs. 4c, 5a). The headland is presently in water depths ranging from 1.5 to 3 m but was emergent during the EBA to EIA (Riddick et al., 2022a). The headland and eastern breakwater define a roughly rectangular eastern harbour basin with an area of about 0.6 ha (EHB; Fig. 5a).

The inshore area (5–10 m depth) beyond the modern harbour preserves relict river channels (Fig. 3) that were formed during the Neolithic (ca. 6500 BCE) when sea levels were > 12 m below present. The channels record a low-gradient river floodplain with a river mouth located in the western Archaic harbour basin (Riddick et al., 2022a). The presence of an active river mouth with wetlands and freshwater resources was likely a key factor in the founding of prehistoric Liman Tepe and Clazomenae at this location on the coast.

4.1.2. Magnetics

The eastern breakwater structure is defined by two curvilinear magnetic lineaments (∼ 20–40 nT) that extend northwest from the headland (Fig. 5b). The anomalies terminate at a magnetic high that underlies the pier structure at the northwestern end of the breakwater. The anomalies do not conform with the rectilinear outline of the breakwater structure, or the wall features on the surface, which suggests the presence of a pre-existing structure at depth within the Archaic breakwater. The linear stone courses visible on the eastern breakwater surface (Fig. 4b) have no apparent magnetic response (Fig. 5b). These appear to be surface constructions composed of low-susceptibility materials (i.e. limestones) that do not extend to depth within the breakwater.

Three distinct zones of high magnetic intensity are located to the west and northeast of the eastern breakwater (Fig. 5b). These zones may indicate the presence of ship refuse (e.g., clay pottery) and ballast materials (Boyce et al., 2009), or areas where the more highly magnetized volcanic bedrock is close to the seabed (Kayan et al., 2019). To the west of the eastern breakwater, a 60–70 nT positive magnetic anomaly coincides with the pier structure and thick Archaic to Roman-age harbour basin deposits. Recent underwater excavations in trenches E and F (Fig. 2b) have uncovered a thick (>3 m) sequence of harbour sediments and pottery refuse, including large *pithoi* fragments and abundant ballast stones (Tuğcu, 2017).

4.2. Elemental geochemistry

Seven distinct lithochemofacies (LC-1 to 7) were identified and correlated across a west-east core transect (Figs. 6a, 7). The Pearson correlation coefficients for selected elements in core 17–9 are shown as correlograms in Fig. 6b. The r values were calculated separately for the upper and lower portions of the core (4.60–5.29 m and 5.30–6.61 m respectively) as the uppermost lithochemofacies LC-5 contrasted significantly in texture and elemental composition with the underlying units (Fig. 6a). The terrigenous elements (Al, Si, K, Ti, Fe) in LC-5 were moderate to strongly correlated ($r = 0.42$–0.91) (Fig. 6b). The strong association between K, Ti and Fe ($r = 0.61$–0.91) is interpreted as clay minerals in sediments derived by weathering of the local volcanic bedrock (Riddick et al., 2022a). Ti in sediments can include detrital (crystalline) Fe-Ti-oxide phases (e.g. ilmenite, titanomagnetite) and Ti substituents in clay minerals (e.g. kaolinite) (Skrabal and Terry, 2002). Colloidal Ti-oxides (e.g. $TiO(OH)_2$) produced by weathering of Fe-Ti-oxide minerals are also incorporated into clays and adsorbed onto organic particles (Morad and Adin Aldahan, 1986; Skrabal and Terry, 2002). Ca and Sr showed a strong correlation within shell-rich horizons in LC-3 and LC-4 ($r = 0.61$) but had no significant correlation in LC-5 (Fig. 6b), which had an overall low content of shell materials. Br, an indicator of marine organic matter content (Ziegler et al., 2008; Seki et al., 2019), showed discrete abundance peaks within *Posidonia* seagrass matte layers in LC-4 (Fig. 6a). Br was anti-correlated with Ca and Sr and positively correlated with Ti and Fe, indicating an association between marine plant organic content and more clay-rich sediment facies (Fig. 6b). S showed a positive correlation with terrigenous elements (Al, Si, K, Ti) in LC-5 and a strong correlation with Fe ($r = 0.82$–0.85) throughout the core. S is present in marine organic matter and in Fe-sulfides produced under anoxic conditions in marine

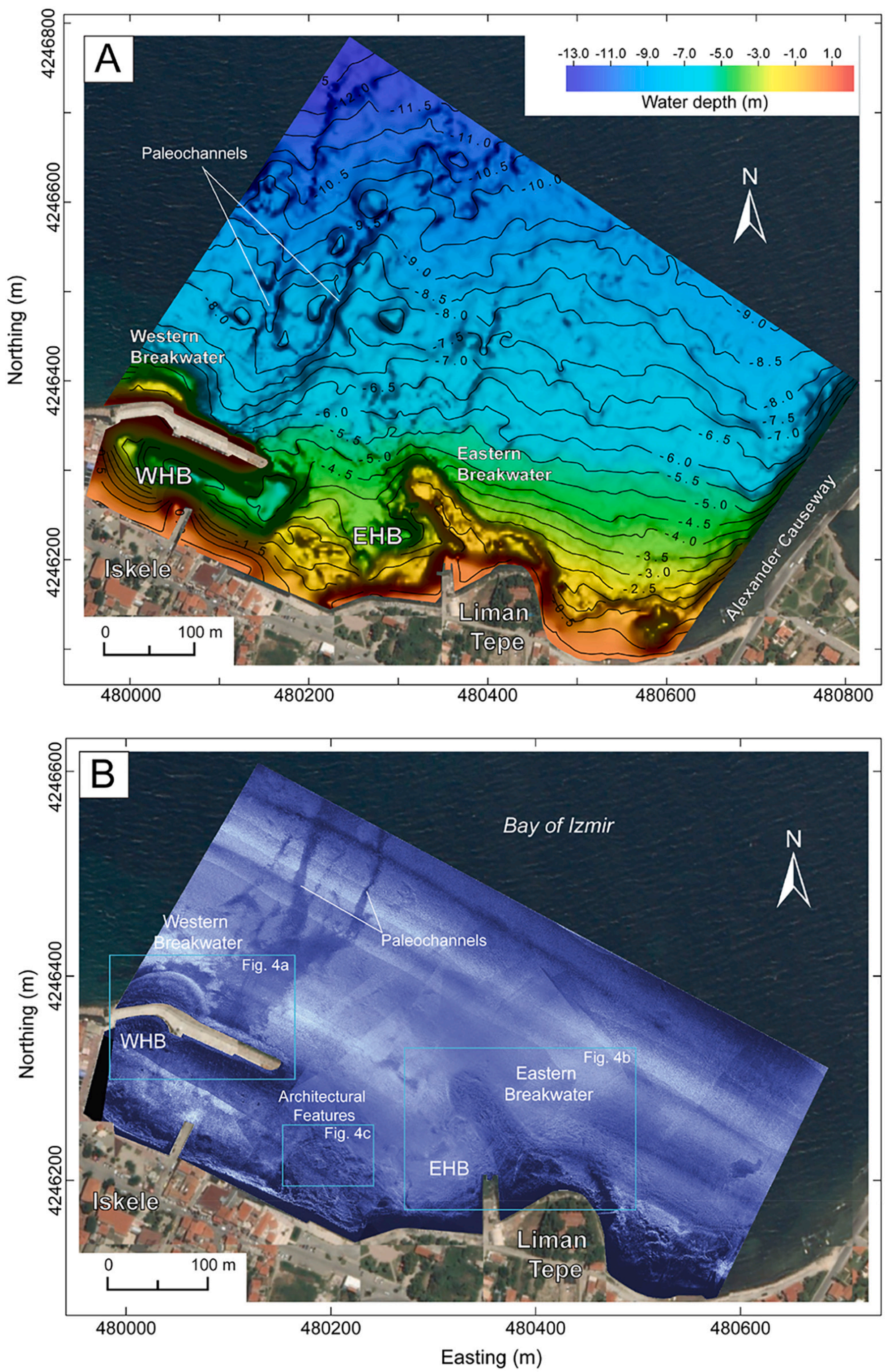

Fig. 3. A. Bathymetry map of inshore survey area and Archaic harbour basins (0.5 m contours). WHB = western harbour basin, EHB = eastern harbour basin. Northeast-trending palaeochannels record a drowned Neolithic alluvial plain (Riddick et al., 2022a) with an active river mouth in the WHB during the Bronze Age and Iron Age settlement phases. B. Side-scan sonar mosaic showing submerged harbour breakwater structures and locations of high-resolution side-scan images shown in Fig. 4.

sediments (Fig. 6b) (Rothwell and Croudace, 2015). Ti and Ca were anti-correlated throughout core 17–9 ($r = -0.32$ to -0.53), supporting the use of the Ti/Ca ratio as a relative indicator of terrigenous versus biogenic sediment inputs (Rothwell and Croudace, 2015).

In the lower half of core 17–9 (5.3–6.61 m), elemental abundances were more variable, reflecting the greater lithofacies heterogeneity in lithochemofacies LC-3 and LC-4 (Fig. 6a, b). K and Si were strongly correlated ($r = 0.91$) and Fe showed little or no correlation with Al, Si or K, but was strongly correlated with Ti ($r = 0.66$) and S ($r = 0.82$) (Fig. 6b). This suggests that Fe and Ti in LC-3 and LC-4 are dominantly detrital Fe-Ti-oxide phases (e.g. ilmenite, titanomagnetite) and not substituents of aluminosilicate clay minerals (Fig. 6a).

4.2.1. LC-1 (terrestrial clays)

LC-1 was a dark grey, compact basal clay in core 19–1, containing abundant angular rock fragments (20–50%) derived from local volcanic

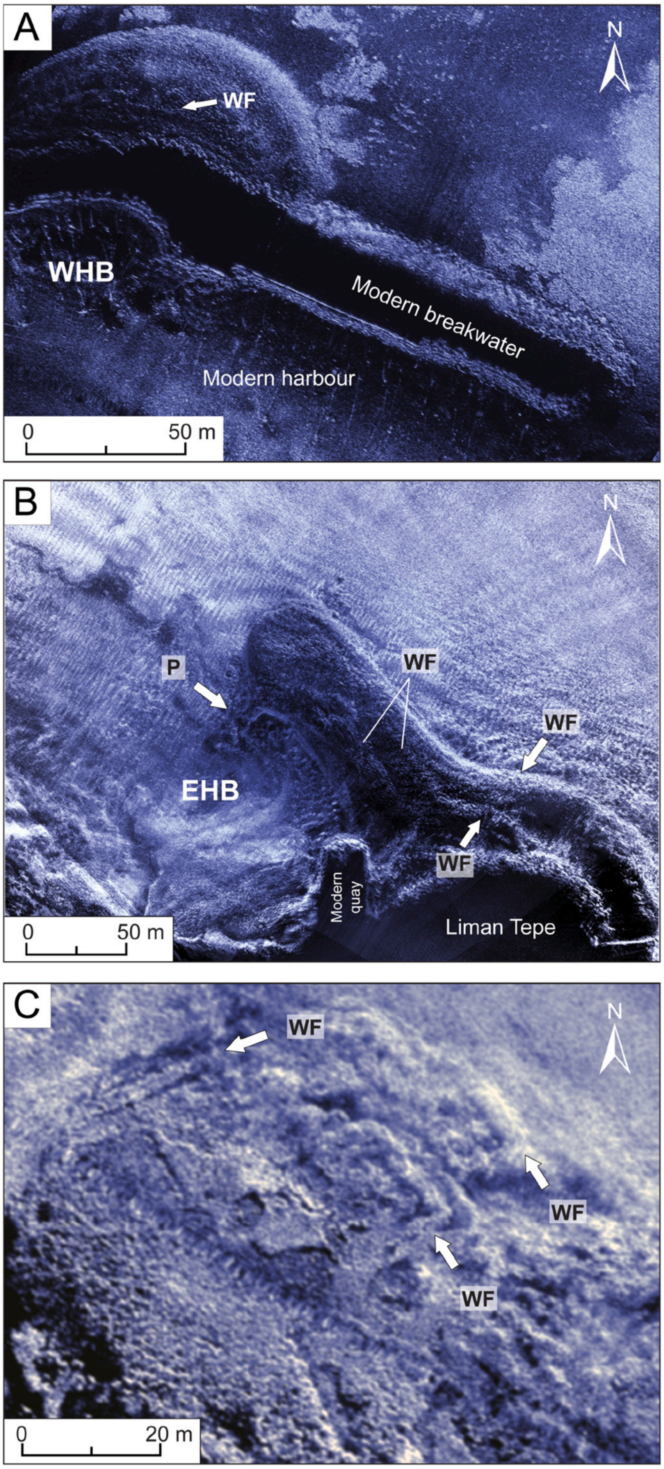

Fig. 4. A. Side-scan sonar mosaics (locations in Fig. 3b): A. Western breakwater showing remains of arcuate wall features (WF) on surface. B. Eastern breakwater structure showing linear pier (P) at northwestern tip of breakwater and linear wall features (WF) on breakwater surface. Breakwater is contiguous with broad (>5 m wide), semi-circular wall feature at the base of the headland, representing a possible seawall or fortification wall. C. Recti-linear backscatter patterns indicating wall features on submerged headland to west of eastern breakwater. The headland was emergent during the LBA to EIA and divided the harbour into eastern and western basins.

bedrock (middle Miocene Menteş trachyte; Kaya, 1979; Göktaş, 2016) (Fig. 7). The clay was devoid of foraminifera and marine molluscs and contained a low abundance of *Difflugid* thecamoebians (Riddick et al., 2022a). The clay had a high abundance of terrigenous elements (Al, K, Si, Ti, Fe) and Ca was depleted. The Ti/Ca ratio was an order of magnitude greater than in the overlying marine sediments (core 19–1; Fig. 7). The absence of marine fauna, inclusions of weathered volcanic bedrock, and abundance of lithogenic elements indicate that LC-1 is a terrigenous clay derived by sub-aerial weathering of volcanic bedrock (Riddick et al., 2022a). A ^{14}C date at the top of LC-1 yielded a Neolithic age of 7042–6747 cal. BCE (Fig. 7).

4.2.2. LC-2 (lagoon, coastal pond)

LC-2 was a laminated clayey silt with low organic content (core 19–1; Fig. 7). Foraminifera abundance was low at the base (<80/cc), increased up core (>160/cc) and was dominantly *Ammonia* and *Elphidium* spp. *Difflugid* thecamoebians were present at the base of LC-2 in core 19–1 (7.05 m depth), where a bulk organic sample yielded a Neolithic age (6238–6070 cal. BCE) (Fig. 7). LC-2 was deposited in a low-energy lagoon or coastal lake environment, transitional with the foreshore marine deposits of overlying LC-3 (Fig. 7). The increase in Ca and foraminifera and decline in Ti/Ca at the base of LC-2 has been interpreted as a marine transgressive surface (Wolters et al., 2010), recording the mid-Holocene inundation of the coastal plain (Riddick et al., 2022a).

4.2.3. LC-3 (foreshore-upper shoreface)

LC-3 was poorly-sorted, gravelly sand with abundant marine mollusc fragments (e.g. *Bittium* sp., *Alvania* sp.) and abundant foraminifera (342–432/cc; *Ammonia* and *Elphidium* spp.). Marine organics from LC-3 in core 17–9 dated to 3630–3142 cal. BCE (Middle to Late Chalcolithic) and 4940–4449 cal. BCE (Early to Middle Chalcolithic) in core 19–2 (Figs. 6, 7). LC-3 was defined lithochemically by increasing Ca relative to Si and Ti and decreased Ti/Ca (Figs. 6, 7). Br was low, indicating a low content of marine plant organic matter (Fig. 6). LC-3 is interpreted as a high-energy, foreshore to upper shoreface environment and is correlated with the upper shoreface deposits and *Elphidium-Ammonia* biofacies of Goodman et al. (2009) (core G-22; Fig. 8). A gastropod shell (*Bittium* sp.) sample near the base of core G-22 (7.7 m bsl) yielded an Early to Middle Chalcolithic age of 5048–4531 cal. BCE for the shoreface deposits, consistent with the age obtained in core 19–2 (Figs. 7, 8).

4.2.4. LC-4 (shoreface)

LC-4 was a crudely bedded, silty sand with abundant foraminifera (496–675/cc), marine shell fragments and *P. oceanica* roots and matte layers up to 10 cm in thickness (Fig. 6a). The dominant foraminifera taxa were *Ammonia* and *Elphidium* spp. LC-4 contained the most diverse assemblage of marine shells, including abundant gastropods (e.g. *Bittium reticulatum*, *Alvania cancellate, Cyclope neritea*) and bivalves (*Astarte* spp., *Cerastoderma* spp.) common to shallow marine inshore environments (Öztürk et al., 2014). Two dates from core 19–1 (bivalve shell and *P. oceanica*) yielded ages of 5113–4605 cal. BCE (Early to Middle Chalcolithic) and 1684–1181 cal. BCE (MBA to EIA) in LC-4 (Fig. 7). Dates from core 17–9 ranged between 3312-2778 cal. BCE (Late Chalcolithic to EBA) and 1816–1308 cal. BCE (MBA) (Figs. 6, 7). In core 17–9, Si and Ti abundances generally increased upward in LC-4 and Br was highly variable with peak values within organic-rich *Posidonia* matte layers (Fig. 6a). Br and Ca values were anti-correlated ($r = -0.57$; Fig. 6b) reflecting changes in the relative abundance of mollusc shell debris and marine plant organic matter in the sediments (Fig. 6a).

The abundance of foraminifera (*Ammonia* and *Elphidium* spp.), marine mollusc fragments and *Posidonia* matte layers indicate that LC-4 represents a shallow marine shoreface environment (Fig. 6a). LC-4 correlates with the onset of the *Brizalina* biofacies (15–20% *Bolivinid* spp.) previously identified at 5.2–6.25 m depth in core G-22 (Goodman et al., 2009) in the eastern harbour basin (Fig. 8). This biofacies was

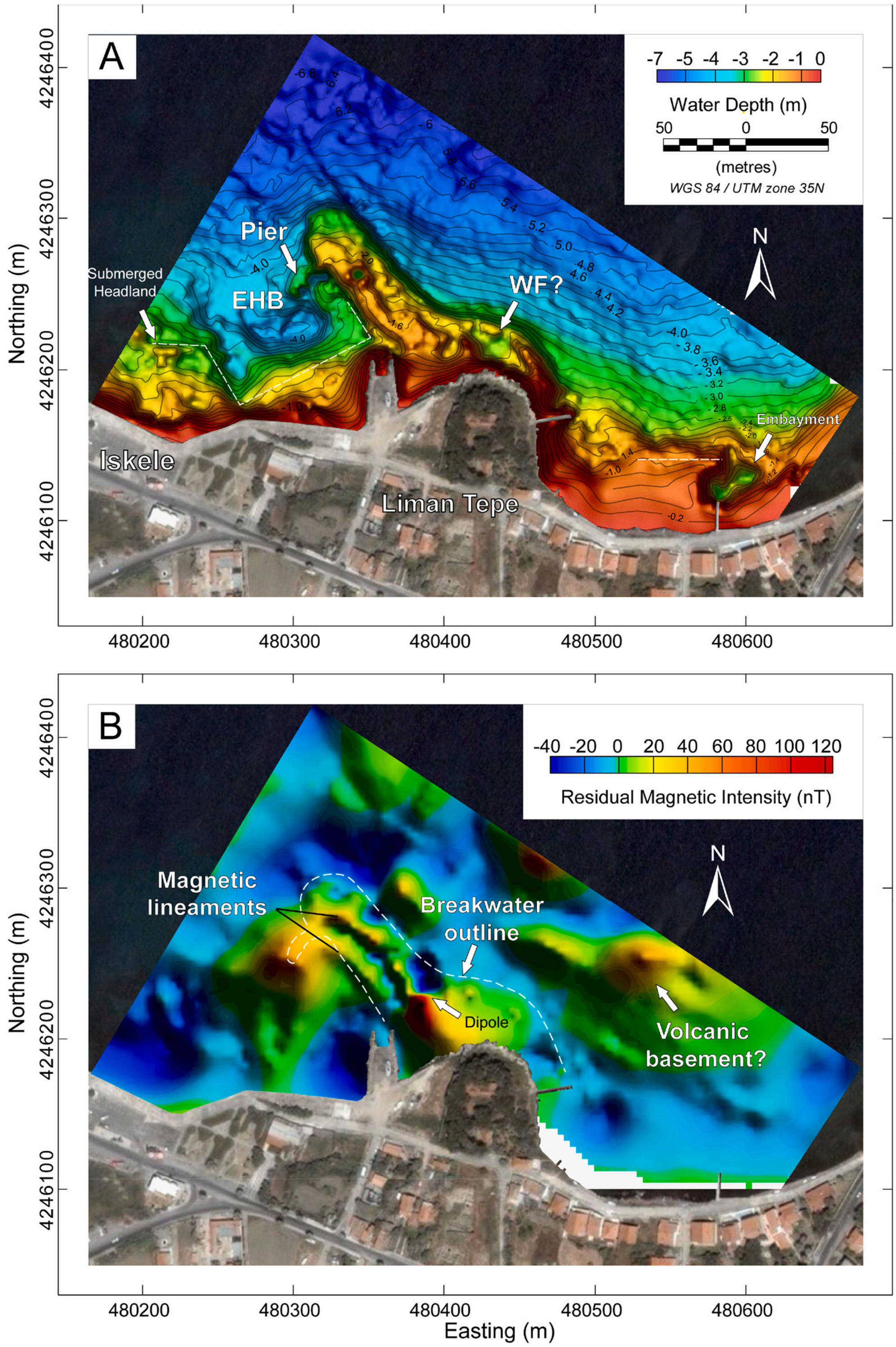

Fig. 5. A. Bathymetry map of eastern harbour basin (EHB) (contour interval 0.2 m). Breakwater is contiguous with a semi-circular wall feature (WF), indicating possible seawall or fortification wall. B. Residual magnetic intensity map for same area, showing arcuate, northwest-trending magnetic lineaments (~20–40 nT) within the eastern breakwater structure. Dashed line shows outline of Archaic harbour breakwater.

interpreted as the onset of a eutrophic Archaic harbour environment, but new AMS ^{14}C dates show that LC-4 sediments span the Late Chalcolithic to Late Bronze Age (ca. 3100–1300 BCE) (Figs. 6a, 8). We re-interpret the *Brizalina* biofacies in cores 17–9 and G-22 as signaling the increasing eutrophication of shallow marine shoreface environments at Liman Tepe, during a phase of settlement expansion and population growth that began in the Late Chalcolithic to EBA (Tuncel and Şahoğlu, 2018). The environmental shift is also recorded by a gradual, upward increasing trend in Ti, Si, K, Fe and Ti/Ca (Figs. 6a, 7), signaling increased terrigenous sediment inputs to nearshore marine environments (Enters et al., 2010; Roberts et al., 2019).

4.2.5. LC-5 (sheltered embayment and Archaic harbour basin)

LC-5 was distinctive, crudely laminated, organic-rich muddy silt

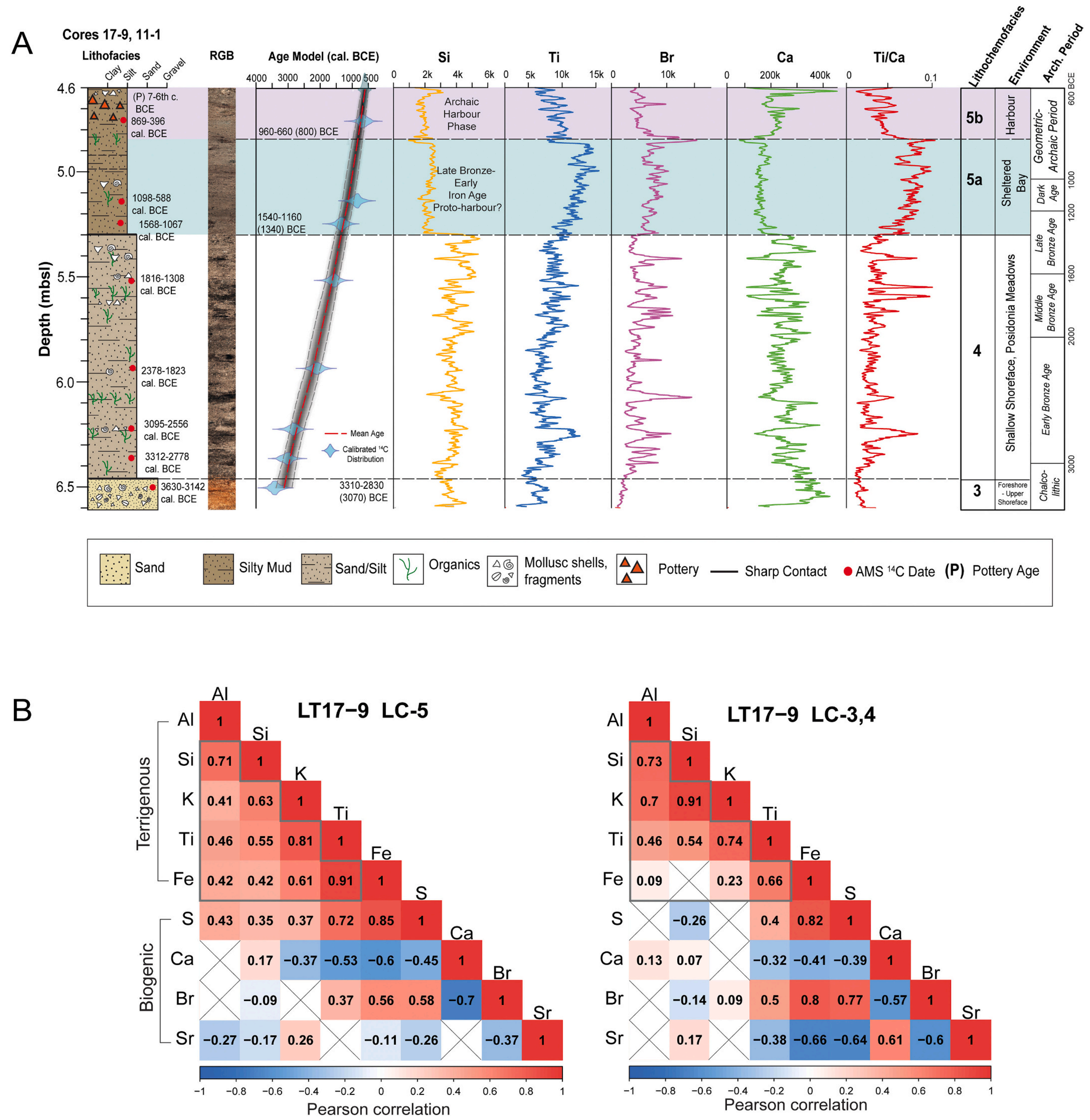

Fig. 6. *A. Core* 17–9 lithostratigraphy, RGB core scan, age-depth model and XRF element profiles. B. Correlation heatmaps (Pearson's r, α = 0.01) for selected elements from core17–9 units LC-5 (4.6–5.29 m) and LC-3, 4 (5.3–6.61 m). All correlations have *p*-values <0.01 except blank cells, which were rejected at the 99% significance level. Terrigenous element correlations outlined in grey for comparison.

facies with abundant foraminifera (374–1094 /cc). The dominant taxa were *Ammonia, Elphidium, Rosalina,* and *Bolivina* spp. LC-5 had a much lower content of mollusc shell debris compared with LC-4. The dominant molluscs included *Bittium* and *Gibbula* spp. gastropods (e.g. *B. reticulatum*, G. *adansonii*) and the bivalves *Parvicardium exiguum*, *Loripes lacteus* and *Venus verrucosa*. *P. exiguum* and *L. lacteus* are common bivalves found in shallow, sheltered lagoons and in ancient harbours with fine-grained sediments (Marriner and Morhange, 2007). In contrast to LC-4, shell materials showed a low degree of taphonomic alteration and the preservation of articulated, whole bivalve shells (e.g. *P. exiguum, V. verrucosa*). The abundance of *P. oceanica* seagrass matte layers showed a major decline at the LC-4/LC-5 boundary and LC-5 contained only thin lenses and seagrass leaf fragments (Fig. 6a).

LC-5 was further sub-divided into two distinct lithochemofacies (Figs. 6, 7). LC-5a was defined by a basin-wide increase in Ti/Ca and decrease in Si within a distinct sandy silt facies (Fig. 6a). The grain size shift from sand to silt, decrease in *Posidonia* matte layers, and increase in Ti/Ca in LC-5a, indicates a transition from an upper shoreface environment (LC-4) to a sheltered, marine embayment with increasing terrigenous sediment inputs. The sharp decrease in Si (> 50% peak area)

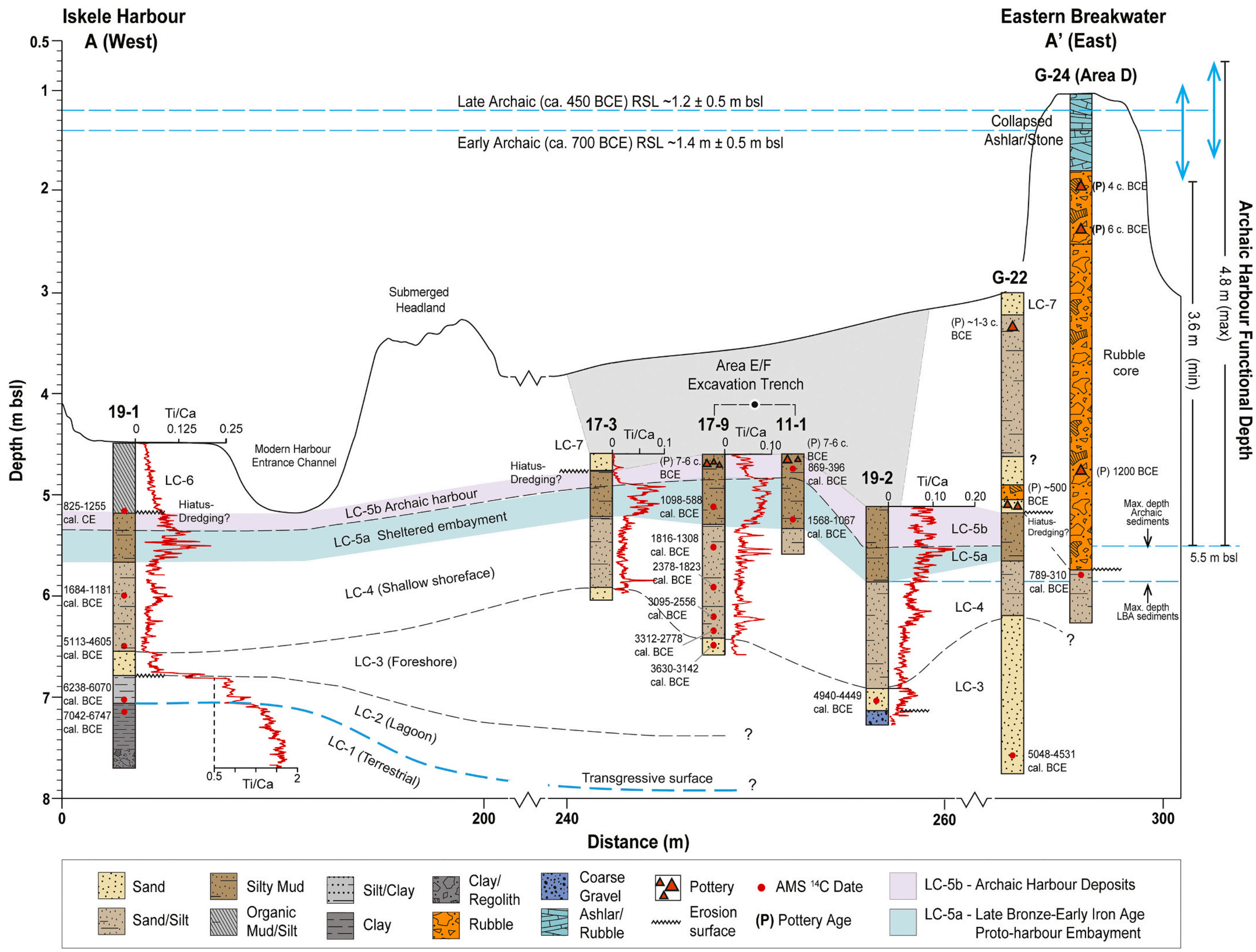

Fig. 7. West-east core transect (A-A'; Figs. 1a, 2a) showing core lithofacies, Ti/Ca profiles, AMS ^{14}C dates and correlated lithochemofacies (LC 1–7). Cores 17–9 and 11–1 were collected at the same location in trench E/F (Fig. 2a). Archaic harbour functional depth estimated from RSL curve (Fig. 10) and maximum depth of Archaic harbour deposits (LC-5b).

and increase in Ti is interpreted as a reduction in sand transport to the marine embayment by longshore processes and increased terrigenous sediment delivery to the coast during the LBA to EIA (1540–1160 cal. BCE) (Fig. 6a). LC-5a correlates with a rise in *Bolivinid* spp. in cores 17–9 and G-22 (*Brizalina* biofacies), which signals a shift to a lower energy, eutrophic marine environment (Goodman et al., 2009) (Fig. 8).

LC-5b was a muddy silt unit defined lithochemically by a sharp decrease Ti/Ca in all cores (increase in Ca relative to Ti) during the Geometric to early Archaic periods (960–660 cal. BCE) (Fig. 6a). The decline in Ti/Ca corresponds with the base of Archaic harbour floor deposits in excavation trenches (~4.6–4.8 m bsl) (Tuğcu, 2017). LC-5b correlates with the *Rosalina* biofacies identified by Goodman et al. (2009) in core G-22 (Fig. 8) and the appearance of Archaic (7th-6th c. BCE) pottery in core 17–9 (Fig. 6a). LC-5b is interpreted as harbour silt and mud deposits accumulated in the low energy environment of the eastern harbour basin (EHB; Fig. 5a).

4.2.6. LC-6, 7 (Byzantine-modern harbour)

LC-6 consisted of a silty mud, overlying LC-5 across a sharp, erosive contact in core 19–1 (Fig. 7). LC-6 had abundant foraminifera, including *Elphidium* and *Miliolids* spp. (877/cc). Organics at the basal contact yielded an age of 825–1255 cal. CE. LC-6 is interpreted as harbour mud deposited in Ottoman to recent (modern) harbour environment (Fig. 7).

LC-7 was a thin (< 20 cm), coarse gravelly sand with abundant mollusc shell fragments and low Ti/Ca at the top of cores 17–3 and G-22 (Fig. 7). LC-7 represents modern upper shoreface sand and gravel accumulating in the modern harbour basin.

5. Discussion

5.1. Coastal palaeoenvironments and harbour phases

5.1.1. Late Bronze-Early Iron Age proto-harbour

The distinct shift in lithochemofacies and grainsize at the LC-4/LC-5 boundary (Figs. 6, 7) indicates a transition from a sandy shoreface environment to a sheltered marine-estuarine embayment (Fig. 9a). The transition is marked by a decrease in grain size and Si and an increase in Ti and other detrital elements (e.g. Al, K, Fe). The Ti/Ca profile shows a distinct upward increase in LC-5a that is a basin-wide signal in all cores (Fig. 7), indicating increased terrigenous sediment flux to the embayment relative to biogenic $CaCO_3$ production (Ziegler et al., 2008; Rothwell and Croudace, 2015; Pint et al., 2015; Seki et al., 2019; Riddick et al., 2022a). Terrigenous sediments were derived from streams draining a low-relief coastal plain and wetlands and by overland flow from the nearby Bronze Age settlement (Fig. 9a). The area to the west of Liman Tepe is underlain by volcanic bedrock, which is the local source of

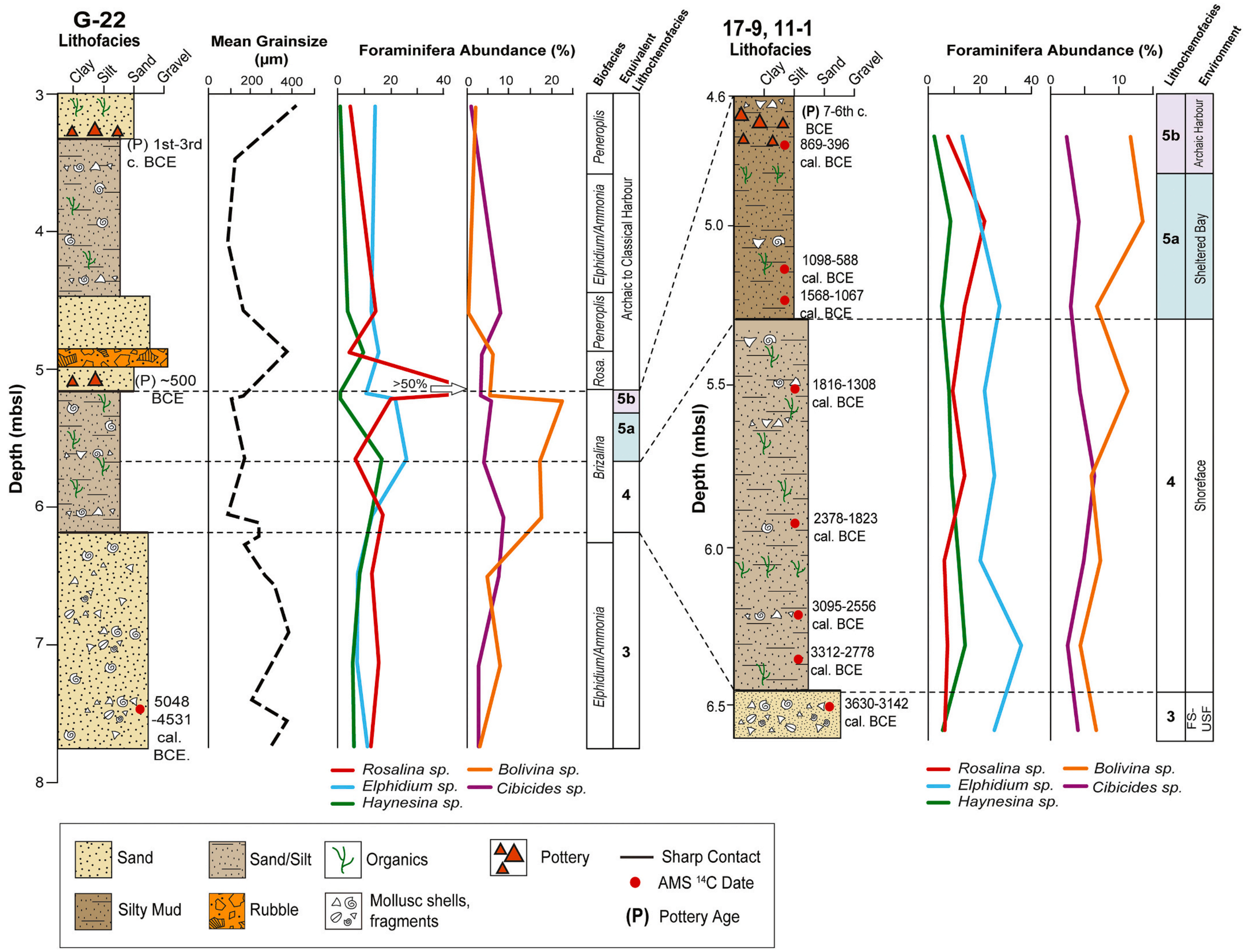

Fig. 8. Correlation of core 17–9 lithostratigraphy and foraminifera with core G-22 of Goodman et al. (2009). Marine foreshore and shoreface sands (LC-3, 4) are dominated by *Elphidium/Ammonia* spp. The rise in *Bolivina* and *Cibicides* spp. (LC-4, 5; *Brizalina* biofacies) indicates increasing eutrophication of marine waters, signaling a phase of settlement expansion in the Late Chalcolithic to Early Bronze Age (EBA). The onset of the Archaic harbour phase (ca. 7th c. BCE) is indicated by an increase in *Rosalina* biofacies at ~5.2 mbsl in core G-22.

detrital elements and clay minerals (Kayan et al., 2019; Riddick et al., 2022a). The terrestrial clays at the base of core 19–1 (LC-1; Fig. 7) are the product of subaerial weathering of trachytic-andesite, which produces Fe- and Ti-oxide rich soils.

The gradual rise in Ti/Ca in LC-5a is interpreted as a signal of increasing soil erosion and terrigenous sediment input to the coastal embayment during the LBA to EIA (Figs. 6, 9a) (Van Andel et al., 1990; Enters et al., 2010; Roberts et al., 2019). The Bronze Age building techniques at Liman Tepe employed dry stone masonry and wattle-and-daub construction using mud bricks made from local clay deposits (Tuncel and Şahoğlu, 2018). The increased terrigenous sediment influx to the coastal embayment (Fig. 7) could record LBA and EIA land disturbances associated with settlement expansion and agricultural development around the headland (Fig. 2a). The shift to finer grain size (Fig. 6a) and a marked decrease in the abundance of *P. oceanica* in LC-5a indicates a more turbid, low-energy embayment that did not support seagrass growth (Pasqualini et al., 1998; García-Márquez et al., 2022). The LBA palaeogeography (Fig. 9a) suggests an embayment formed in the lee of the Liman Tepe headland, or possibly a tombolo, formed by westward longshore sediment transport along the coast (Riddick et al., 2022a). Tombolo formation may have been promoted by the presence of submerged bedrock 'knolls' in the inshore area to the northwest of the headland (Goodman et al., 2009). The embayment in the lee of the headland would have provided a sheltered anchorage area during the LBA to EIA (Riddick et al., 2022a).

The distinct environmental shift at the LC-4/LC-5 boundary (Fig. 6a) could also indicate augmentation of the proto-harbour embayment by construction of a pier or breakwater from the Liman Tepe headland (Fig. 9a). The sharp decline in both Si and Ca and increase in Ti/Ca at the LC-4/LC-5 boundary (Fig. 6a) suggests decreased longshore sand transport to the basin. Magnetic mapping identified a buried northwest-trending structure at depth within the Archaic breakwater, which does not conform with the rectilinear outline of the mole (Fig. 5b). Its arcuate form, curving towards the west, may indicate a narrow, recurved pier structure built out from the rocky headland and buried below later Iron Age (Archaic) constructions.

5.1.2. *Iron Age harbour (ca. 7th-6th c. BCE)*

The onset of the Archaic harbour construction (Fig. 9b) is signalled by a decrease in Ti/Ca, a shift from a *Brizalina* to *Rosalina* biofacies, and the appearance of Archaic pottery in unit LC-5b (Figs. 7, 8). An AMS ^{14}C date on *Posidonia* from below the breakwater rubble in core G-24 (Fig. 7) suggests a broad *terminus post quem* of 789–310 cal. BCE (median age 546 BCE; table 1) for the breakwater construction. In cores 17–9 and 11-

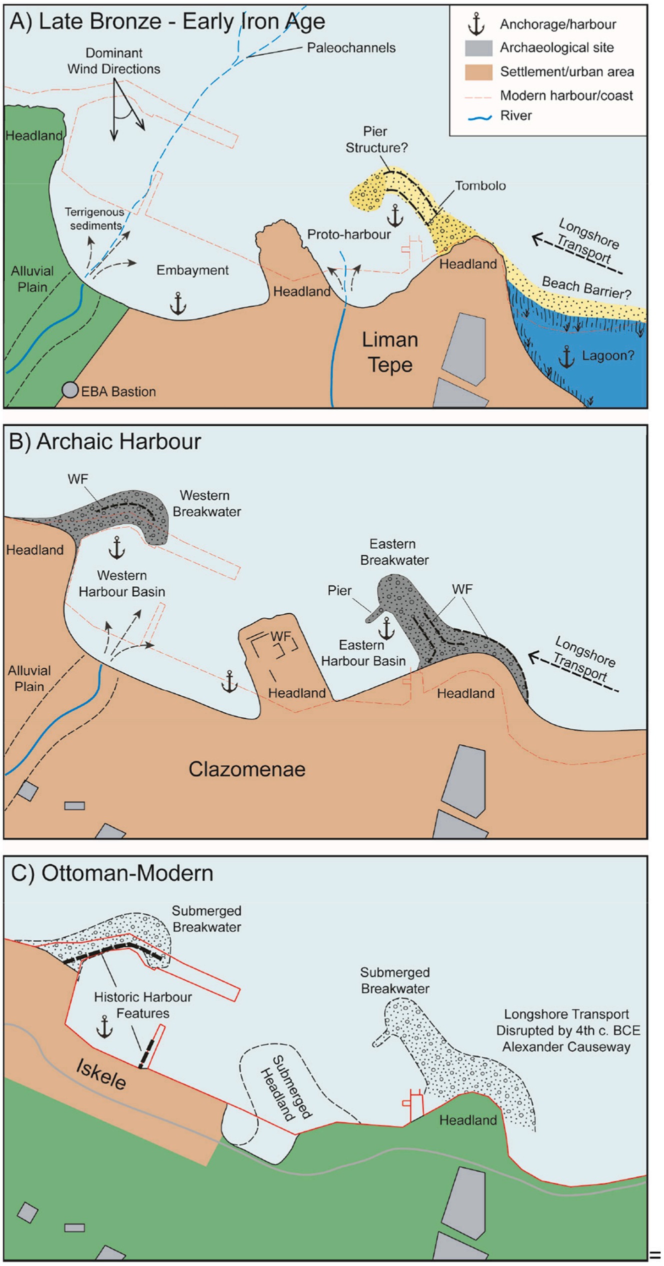

Fig. 9. Palaeo-coastal evolution and harbour development. A. Late Bronze Age (LBA) to Early Iron Age (EIA) proto-harbour phase. Accumulation of terrigenous sediments in sheltered marine embayment in the lee of rocky headlands or tombolo formed by longshore transport. Linear magnetic anomaly patterns (Fig. 5b) may indicate augmentation of the proto-harbour embayment by a narrow pier built out from the headland. B. Archaic (ca. 7th-6th c. BCE) harbour phase. Rubble breakwaters were constructed on top of existing bedrock highs (or tombolo?) to form semi-enclosed harbour basins. The western breakwater and pier structure on eastern breakwater provided anchorage areas protected from the dominant northerly winds. C. Ottoman-modern harbour phase (based on historical photos). Ottoman constructions included two narrow pier structures in the western harbour basin. Photos from the period record dredging in the western harbour basin and backfilling of the shoreline in Iskele harbour (Tuğcu, İ., 2017).

1, the abundance of 7th–6th c. BCE pottery and two AMS ^{14}C dates from immediately below the pottery layer (Fig. 6a; Table 1), including a date on a well-preserved olive seed (652–544 BCE), indicate a more likely 7th-6th c. BCE age for the onset of harbour development (Table 1). The age-depth model, predicts a transition from LC-5a to LC-5b harbour sediments at 960–660 cal BCE (Fig. 6a), consistent with a 7th c. BCE construction date within the range of ^{14}C model errors. The sharp decline in Ti/Ca at the LC-5a to 5b transition indicates a decrease in terrigenous sediment inputs to the harbour basin (Figs. 6a, 7) and is correlated with the onset of the *Rosalina* biofacies in core G-22 (Fig. 8). The *Rosalina* biofacies includes *R. bradyi* (>50%), which prefer rocky or coarse-sand substrates (Avsar and Ergin, 2001; Hayward et al., 2007; Goodman et al., 2009). We interpret the rise in *Rosalina* spp. as the colonization of hardgrounds provided by the breakwater rubble. The decrease in Ti/Ca in LC-5b indicates increasing marine influence and a reduction in terrigenous sediment delivery to the eastern harbour basin during the early Archaic Period (Fig. 7).

5.2. *Harbour layout and function*

Geophysical mapping identifies two breakwater structures enclosing a harbour with a total area of >5 ha (Fig. 9b). The harbour was subdivided into two separate sub-basins by an emergent headland lying to the east of an active river mouth (Figs. 3b, 9b). The eastern breakwater was built out from the Liman Tepe headland by the piling of rubble directly onto the seabed (Figs. 4a, 9b). The western breakwater was constructed using similar methods to form a ~ 150 m long, recurved mole, with a sheltered basin in its lee side (Fig. 9b). Using the average rubble thickness (~4 m; G-24; Fig. 7) and eastern breakwater dimensions (~35 × 120 m) and assuming a 40% porosity for coarse quarry stone (Hudson, 1959), it is estimated that on the order 1 × 10^4 m^3 of rubble and fill materials were required for the eastern breakwater construction. The western breakwater, with an estimated surface area of about 7000 m^2 (Fig. 9b), would have required about 1.7 × 10^4 m^3 of quarried stone materials. The harbour construction thus required the quarrying, transport and emplacement of a large volume (~2.7 × 10^4 m^3) of stone and other fill materials. Evidence from excavations (Fig. 2b) and the overall low magnetic intensity of the eastern breakwater (Fig. 5b), confirm that the rubble composition is dominantly limestone, sourced from local Neogene carbonate bedrock. Well-defined linear magnetic anomalies within the breakwater also indicate the presence of high magnetic susceptibility materials (volcanic boulders?) at depth within the structure (Fig. 5b). Volcanic cobbles and boulders were used in the construction of the EBA city fortification walls and sourced locally from the middle Miocene volcanic bedrock.

The linear stone accumulations on the breakwater surfaces indicate architectural features on the mole surface, possibly seawalls or the foundation works of harbour buildings (e.g. storehouses, boatsheds) (Fig. 4a, b). The presence of 4th c. BCE pottery below rubble in core G-24 (Area D, 1.7 m bsl; Fig. 7) suggests that some portion of the breakwater was constructed or perhaps renovated during the early Classical Period. The broad (>3 m wide) semi-circular wall feature encircling the base of headland may represent a seawall or an extension of the city fortification walls (Figs. 3, 5a). The magnetic anomalies within the eastern breakwater do not conform with the rectilinear mole outline and suggest a pre-existing structure buried within the breakwater (Fig. 5b). Previous seismic profiling had identified the possible presence of buried structures at depth within the eastern breakwater (Müller et al., 2009). LBA pottery in the lower portion of the rubble (core G-24, ~5 m depth; Fig. 7) may provide further evidence for pre-Archaic augmentation of the embayment with man-made structures (Fig. 9a) or may represent re-use of LBA rubble materials. Further investigations (i.e., geophysics, excavations) are needed to determine the origin and age of buried structures identified by magnetic mapping, but we speculate that the magnetic anomaly patterns (Fig. 5b) represent a narrow pier built out from the headland, perhaps on top of a pre-existing tombolo (Fig. 9a) (Goodman et al., 2008). The buried structure, if Late Bronze in age, would represent one of the first examples of pre-Iron Age engineered harbour constructions in the Aegean.

The functional depth of the eastern Archaic harbour basin was estimated using the relative sea level (RSL) curve of Riddick et al. (2022a)

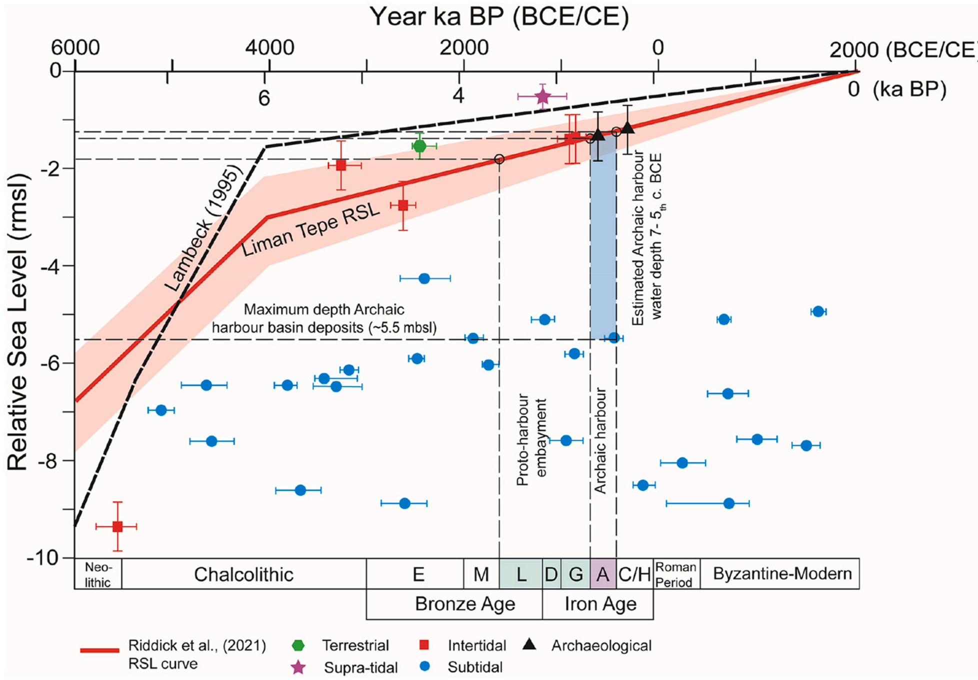

Fig. 10. Relative sea level (RSL) curve for Liman Tepe-Clazomenae (modified from Riddick et al., 2022a) with Lambeck's (1995) glacio-hydro-isostatically corrected eustatic sea level model for comparison. Archaic harbour depth (~4–5 m) estimated from RSL curve and maximum depth of 7th c. BCE harbour floor deposits (5.5. m bsl; Fig. 7).

(Fig. 10). During the Archaic Period (ca. 8th–5th c. BCE) RSL was ~1–1.5 m lower than present. The lowermost limit of Archaic harbour floor sediments in the eastern basin (~5.5 mbsl) and current elevation of the eastern breakwater (1–1.5 mbsl) suggests a functional harbour depth in the range of ~4–5 m during the Archaic Period (Fig. 7). The modern elevation of the eastern breakwater provides a minimum estimate of the original mole surface height, as it has been reduced by wave erosion (de Graauw, 2014). Linear wall features on the breakwater surface (Fig. 4a, b) indicate a superstructure built on top of the breakwater, which would have further elevated the mole height.

The wide separation of the harbour breakwaters (> 200 m) and semi-enclosed harbour basins (Fig. 9b) may have been designed to allow river outflow and limit siltation of the harbour basins by fluvial sediments. The northwest-southeast orientation of the eastern breakwater indicates that it was built out from a pre-existing rocky headland or tombolo. Its orientation suggests that it may have been engineered in part, to prevent siltation of the harbour basins by east-west longshore currents (Figs. 1b, 9b). The narrow pier structure on the northwestern tip of the breakwater was built to provide a small, sheltered basin, protected from the prevailing northerly winds. The harbour basin in the lee of the more extensive western breakwater (~150 m length) would have provided a larger (> 1 ha), well-protected anchorage area (Fig. 9b).

The Archaic harbour (>5 ha) was comparable in size and water depth to the large artificial Roman harbour on the west side of Karantina Island (Fig. 1a), indicating a similar capacity as a trading port. The mainland harbour served as Clazomenae's commercial port, as is evident in the wealth of pottery refuse (Figs. 2c, d), which indicates intensive harbour use during the 7th–6th c. BCE and again in the early Classical Period (4th c. BCE) (Erkanal, 2014a). The gap in harbour use between the 6th and 4th c. BCE was attributed to the migration of the settlement to Karantina Island during the conflict with Persian Empire. The division of the harbour into two separate basins (Fig. 9b) could indicate a level of organization of the harbour facilities. The abundance and thickness of pottery refuse in the eastern harbour basin, which includes large early Classical Period *pithoi* suggests its purpose as a commercial terminus and transhipment port.

5.2.1. *Harbour dredging?*

The truncation of Archaic harbour deposits (LC-5b) below younger sediments in cores 19–1 and G–22 may provide evidence for harbour dredging and maintenance activities (Fig. 7). Harbour dredge spoils and anthropogenic sediments (ballast deposits, pottery refuse) are a common feature of ancient harbour deposits (Marriner and Morhange, 2007; Morhange and Marriner, 2010; Riddick et al., 2021). In core 19–1, the age of the LC-6 basal mud (825–1255 CE) indicates a significant hiatus and dredging of the western basin to the depth of the modern entrance channel (~5.2 m bsl) (Fig. 7). Historical photos document several phases of harbour renovations and dredging of the western harbour and entrance channel during the Ottoman Period (Tuğcu, 2017). In core G–22, on the western flank of the eastern breakwater (Fig. 2b), early Archaic (ca. 7th c. BCE) harbour deposits of LC-5b are truncated by a coarse sand (4.5–5.2 m bsl) containing 5th c. BCE pottery and a 20-cm-thick rubble layer (Figs. 7, 8). The apparent ~200-year erosional hiatus at the base of the sand indicates possible dredging of the small basin to the south of the breakwater pier during the late Archaic (Fig. 2b). The poorly-sorted rubble layer could also represent a ballast stone accumulation or slumping of the western edge of the mole structure. The continuous sediment record from core 17–9 shows no evidence for erosional hiatuses or anthropogenic sediments below the pottery-rich layers in the upper 20 cm of LC-5b (Fig. 6a). This suggests that dredging was not employed in the early Archaic phase of harbour development but does not rule out sediment dredging during later phases of the Iron Age harbour. Harbour basin dredging may not have been required during the early harbour phase (Fig. 9b) due to the water depth (~4–5 m) and the limited sand inputs to the basin, as indicated by the fine-grained silty texture of the Archaic harbour sediments (Figs. 6a, 7).

6. Summary

In the Aegean, coastal embayments and lagoons provided anchorage sites until the EIA, when engineered structures (e.g., breakwaters, quays) were built to enhance and protect natural harbours (Marriner et al., 2010; Tartaron, 2013; Mauro, 2019; Mauro and Gambash, 2020). At Liman Tepe-Clazomenae, one of the best-preserved Iron Age harbours in the eastern Aegean, the transition from a natural proto-harbour embayment to semi-enclosed, engineered harbour is recorded by changes in sediment elemental geochemistry and foraminifera within a distinctive silty mud chemofacies (Figs. 6, 8). The transition is marked by a decline in Si and rise in Ti/Ca, defining a basin-wide lithochemical boundary (Figs. 6, 7), which we interpret as a shift from a marine shoreface environment to a marine-estuarine embayment. The embayment may have formed in the lee of a tombolo attached to the headland or may have been augmented by construction of a pier or seawall (Fig. 9a). Magnetic anomaly patterns indicate a pre-existing buried structure within the eastern Archaic breakwater (Figs. 5b); possibly a pier or seawall constructed to protect the proto-harbour during the LBA to EIA. The onset of Archaic harbour construction in the 7th–6th c. BCE is recorded by a sharp decline in Ti/Ca and a shift to a lower energy, eutrophic harbour environment dominated by a *Rosalina* spp. (Figs. 7, 8). The Archaic harbour breakwaters were constructed by piling of a large volume of coarse rubble onto the seabed to create two semi-enclosed harbour basins (Fig. 9b). The breakwater construction materials were derived mainly from local Neogene carbonate bedrock, but magnetic anomalies indicate the presence of more magnetized, volcanic materials at depth within the eastern mole structure. The harbour was most active during the 7th–6th and 4th centuries BCE and likely served as Clazomenae's principal mainland commercial port.

The results from Liman Tepe-Clazomenae demonstrate that high-resolution XRF core scanning and chemofacies analysis (Figs. 6, 7) can identify palaeoenvironmental changes in ancient harbour sediments that would not be resolved using conventional palaeoecological and sedimentological techniques with decimetric sampling intervals. This paper represents the first use of micro-XRF geochemical records to document the transition from a LBA proto-harbour embayment to semi-enclosed, engineered Early Iron Age harbour basin in the Aegean.

Data availability

Micropalaeontological data used in this study are available online at: https://data.mendeley.com/datasets/fbkv5dj64f/1, an open-source online data repository hosted at Mendeley Data (Riddick et al., 2022b).

Authorship statement

NLR, JIB data analysis, figure drafting, primary writing and revising of the manuscript. NLR, JIB, VŞ and HE - research design and objectives. Fieldwork - NLR, JIB, İT, YA. BNG-T and EGR - core and micro-palaeontological data and interpretations. All authors contributed to data interpretation, writing, and revision of the final manuscript.

Declaration of Competing Interest

The authors declare that they have no known competing financial interests or personal relationships that could have appeared to influence the work reported in this paper.

Acknowledgements

Research work conducted under permits from the Turkish Ministry of Culture and Tourism and funded by a Natural Sciences and Engineering Research Council of Canada (NSERC) Discovery Grant (RGPIN-2014-05829, 2022-05333) to JIB and grants from the Turkish Ministry of Culture and Tourism, Institute for Aegean Prehistory (INSTAP), TÜBİTAK (108 K263, 114 K266) and Ankara University to VŞ and HE. We gratefully acknowledge funding and support of the Turkish Historical Society (TTK), İzmir Metropolitan Municipality, Turkish Institute of Nautical Archaeology (TINA), the Koç Foundation and Urla Municipality. We thank three anonymous reviewers and the editor for their constructive comments and the students and staff of the Ankara University Mustafa V. Koç Center for Maritime Archaeology (ANKÜSAM), Izmir Region Excavations and Research Project (IRERP) for field and logistical support. NLR was supported by a NSERC Canada Graduate Scholarship. We thank Marine Magnetics Corp. for providing magnetometer equipment and Seequent Ltd. for academic software grants. We dedicate this paper to the memory of dear colleague, mentor, and friend Prof. Dr. Hayat Erkanal (1940-2019).

References

Alves, E.Q., Macario, K., Ascough, P., Bronk Ramsey, C., 2018. The worldwide marine radiocarbon reservoir effect: definitions, mechanisms, and prospects. Rev. Geophys. 56 (1), 278–305.

Ascough, P.L., Cook, G.T., Dugmore, A.J., Barber, J., Higney, E., Scott, E.M., 2004. Holocene variations in the Scottish marine radiocarbon reservoir effect. Radiocarbon 46 (2), 611–620.

Avsar, N., Ergin, M., 2001. Spatial distribution of Holocene benthic foraminifera, northeastern Aegean Sea. Int. Geol. Rev. 43 (8), 754–770.

Aytaçlar, N., 2004. The early iron age at Klazomenai. In: Moustaka, A., Skarlatidou, E., Tzannes, M.C., Ersoy, Y. (Eds.), Klazomenai, Teos and Abdera: Metropoleis and Colony. Proceedings of the International Symposium, Abdera, pp. 17–41.

Blaauw, M., Christen, J.A., 2011. Flexible paleoclimate age-depth models using an autoregressive gamma process. Bayesian Anal. 6 (3), 457–474.

Boyce, J.I., Reinhardt, E.G., Raban, A., Pozza, M.R., 2004. Marine magnetic survey of a submerged Roman harbour, Caesarea Maritima, Israel. Int. J. Naut. Archaeol. 33 (1), 122–136.

Boyce, J.I., Reinhardt, E.G., Goodman, B.N., 2009. Magnetic detection of ship ballast deposits and anchorage sites in King Herod's Roman harbour, Caesarea Maritima, Israel. J. Archaeol. Sci. 36 (7), 1516–1526.

Craigie, N.W., 2018. Principles of Elemental Chemostratigraphy: A Practical User Guide. Advances in Oil and Gas Exploration & Production, p. 189.

Crann, C.A., Murseli, S., St-Jean, G., Zhao, X., Clark, I.D., Kieser, W.E., 2017. First status report on radiocarbon sample preparation techniques at the AE Lalonde AMS Laboratory (Ottawa, Canada). Radiocarbon 59 (3), 695–704.

de Graauw, A., 2014. The long-term failure of rubble mound breakwaters. Méditerranée. J. Mediterranean Geogr. 7078. https://mediterranee.revues.org/.

Dickinson, O., 2006. The Aegean from Bronze Age to Iron Age: Continuity and Change between the Twelfth and Eighth Centuries BC. Routledge, 320 p.

Duchêne, H., Fraisse, P., 2001. Le paysage portuaire de la Délos antique: recherches sur les installations maritimes, commerciales et urbaines, p. 93.

Enters, D., Kirilova, E., Lotter, A.F., Lücke, A., Parplies, J., Jahns, S., Kuhn, G., Zolitschka, B., 2010. Climate change and human impact at Sacrower See (NE Germany) during the past 13,000 years: a geochemical record. J. Paleolimnol. 43 (4), 719–737.

Erkanal, H., 2008. Liman Tepe: New light on prehistoric Aegean cultures. In: Erkanal, H., Hauptmann, H., Şahoğlu, V. (Eds.), The Aegean in the Neolithic, Chalcolithic and the Early Bronze Age. Proceedings of the International Symposium, Urla-Izmir, pp. 179–190.

Erkanal, H., 2014a. Klazomenai/Liman Tepe'nin Limanları. In: Pirson, S., Schmidts, F. (Eds.), Harbors and Harbor Cities in the Eastern Mediterranean, pp. 295–303.

Erkanal, H., 2014b. Liman Tepe in the Late Bronze Age. In: Erkanal, A., et al. (Eds.), Batı ve Doğu Akdeniz Geç Tunç Çağı Kültürleri Üzerine Araştırmalar Sempozyumu. Hacettepe Üniversitesi, 2013, Ankara.

Erkanal, H., Tuğcu, İ., Şahoğlu, V., 2014. Underwater Archaeological Excavations at Liman Tepe in 2014, 2. Turkish Institute of Nautical Archaeology, pp. 42–48.

Ersoy, Y., 2004. Klazomenai: 900–500 B.C. history and settlement evidence. In: Moustaka, A., Skarlatidou, E., Tzannes, M.C., Ersoy, Y. (Eds.), Klazomenai, Teos and Abdera: Metropoleis and Colony. Proceedings of the International Symposium, Abdera, pp. 43–76.

Flemming, N.C., 1980. Gigantic harbors in the Levant. Archaeology under water. In: Muckelroy, K. (Ed.), Archaeology under Water: An Atlas of the world's Submerged Sites. McGraw-Hill Book Company, p. 168.

Galili, E., Benjamin, J., Eshed, V., Rosen, B., McCarthy, J., Horwitz, L.K., 2019. A submerged 7000-year-old village and seawall demonstrate earliest known coastal defence against sea-level rise. PLoS One 14 (12), e0222560.

García-Márquez, M.G., Fernández-Juárez, V., Rodríguez-Castañeda, J.C., Agawin, N.S., 2022. Response of *Posidonia oceanica* (L.) Delile and its associated N_2 fixers to different combinations of temperature and light levels. Front. Mar. Sci. 8, 1–19. https://doi.org/10.3389/fmars.2021.757572.

Göktaş, F., 2016. Neogene Stratigraphy of the İzmir-Outer-Bay Islands. Maden Tetkik ve Arama Dergisi 152 (152), 1–24.

Goodman, B.N., 2006. The Paleogeography of Liman Tepe, Turkey: A Multi-Proxy Geoarchaeological Study.. Unpublished PhD thesis McMaster University.

Goodman, B.N., Reinhardt, E.G., Dey, H.W., Boyce, J.I., Schwarcz, H.P., Sahoğlu, V., Erkanal, H., Artzy, M., 2008. Evidence for Holocene marine transgression and shoreline progradation due to barrier development in Iskele, Bay of Izmir, Turkey. J. Coast. Res. 24 (5), 1269–1280.

Goodman, B.N., Reinhardt, E.G., Dey, H.W., Boyce, J.I., Schwarcz, H.P., Sahoğlu, V., Erkanal, H., Artzy, M., 2009. Multi-proxy geoarchaeological study redefines understanding of the paleocoastlines and ancient harbours of Liman Tepe (Iskele, Turkey). Terra Nova 21 (2), 97–104.

Gregory, B.R., Patterson, R.T., Reinhardt, E.G., Galloway, J.M., Roe, H.M., 2019. An evaluation of methodologies for calibrating Itrax X-ray fluorescence counts with ICP-MS concentration data for discrete sediment samples. Chem. Geol. 521, 12–27.
Haggi, A., 2006. Phoenician Atlit and its newly-excavated harbour: a reassessment. Tel Aviv 33 (1), 43–60.
Haggi, A., Artzy, M., 2007. The harbor of Atlit in northern Canaanite/Phoenician context. Near Eastern Archaeol. 70 (2), 75–84.
Hayward, B.W., Grenfell, H.R., Sabaa, A.T., Daymond-King, R., 2007. Biogeography and ecological distribution of shallow-water benthic foraminifera from the Auckland and Campbell Islands, subantarctic southwest Pacific. J. Micropalaeontol. 26 (2), 127–143.
Heaton, T.J., Köhler, P., Butzin, M., Bard, E., Reimer, R.W., Austin, W.E., Ramsey, C.B., Grootes, P.M., Hughen, K.A., Kromer, B., Reimer, P.J., 2020. Marine20 - the marine radiocarbon age calibration curve (0–55,000 cal BP). Radiocarbon 62 (4), 779–820.
Hudson, R.Y., 1959. Laboratory investigation of rubble-mound breakwaters. J. Waterways Harbors Division 85 (3), 93–121.
Kaya, O., 1979. Ortadoğu Ege çöküntüsünün (Neojen) stratigrafisive tektoniği. Türk. Jeol. Kurumu Bül. 22 (1), 35–58.
Kayan, İ., Öner, E., Doğan, M., İlhan, R., Vardar, S., 2019. Holocene paleogeography and geoarchaeological interpretations on the Urla-İskele coastal plain. Ege Coğrafya Dergisi 28 (1), 11–32.
Koster, B., Vött, A., Mathes-Schmidt, M., Reicherter, K., 2015. Geoscientific investigations in search of tsunami deposits in the environs of the Agoulinitsa peatland, Kaiafas Lagoon and Kakovatos (Gulf of Kyparissia, western Peloponnese, Greece). Z. Geomorphol. 59, 125–156.
Krezoski, G., 2008. Paleoenvironmental Reconstruction of Prehistoric Submerged and Coastal Environments at Liman Tepe/Klazomenai, Turkey. Master's thesis. McMaster University, 139 p.
Kylander, M.E., Ampel, L., Wohlfarth, B., Veres, D., 2011. High-resolution X-ray fluorescence core scanning analysis of Les Echets (France) sedimentary sequence: new insights from chemical proxies. J. Quat. Sci. 26 (1), 109–117.
Lambeck, K., 1995. Late Pleistocene and Holocene sea-level change in Greece and south-western Turkey: a separation of eustatic, isostatic and tectonic contributions. Geophys. J. Int. 122 (3), 1022–1044.
Löwemark, L., Bloemsma, M., Croudace, I., Daly, J.S., Edwards, R.J., Francus, P., Galloway, J.M., Gregory, B.R., Huang, J.J.S., Jones, A.F., Kylander, M., 2019. Practical guidelines and recent advances in the Itrax XRF core-scanning procedure. Quat. Int. 514, 16–29.
Marriner, N., Morhange, C., 2007. Geoscience of ancient Mediterranean harbours. Earth Sci. Rev. 80 (3–4), 137–194.
Marriner, N., Morhange, C., Boudagher-Fadel, M., Bourcier, M., Carbonel, P., 2005. Geoarchaeology of Tyre's ancient northern harbour, Phoenicia. J. Archaeol. Sci. 32 (9), 1302–1327.
Marriner, N., Morhange, C., Doumet-Serhal, C., 2006. Geoarchaeology of Sidon's ancient harbours, Phoenicia. J. Archaeol. Sci. 33 (11), 1514–1535.
Marriner, N., Morhange, C., Goiran, J.P., 2010. Coastal and ancient harbour geoarchaeology. Geol. Today 26 (1), 21–27.
Marriner, N., Morhange, C., Kaniewski, D., Carayon, N., 2014. Ancient harbour infrastructure in the Levant: tracking the birth and rise of new forms of anthropogenic pressure. Sci. Rep. 4 (1), 1–11.
Marshall, M.H., Lamb, H.F., Huws, D., Davies, S.J., Bates, R., Bloemendal, J., Boyle, J., Leng, M.J., Umer, M., Bryant, C., 2011. Late Pleistocene and Holocene drought events at Lake Tana, the source of the Blue Nile. Glob. Planet. Chang. 78 (3–4), 147–161.
Mauro, C.M., 2019. Archaic and Classical Harbours of the Greek World: The Aegean and Eastern Ionian Contexts. Archaeopress Publishing Ltd., 128 p.
Mauro, C.M., Gambash, G., 2020. The earliest "Limenes Kleistoi" A comparison between archaeological-geological data and the Periplus of Pseudo-Skylax. In: Revue des études anciennes, 122(1). Université Bordeaux Montaigne, pp. 55–84.
Morad, S., Adin Aldahan, A.L.A., 1986. Alteration of detrital Fe-Ti oxides in sedimentary rocks. Geol. Soc. Am. Bull. 97 (5), 567–578.
Morhange, C., Marriner, N., 2010. Mind the (stratigraphic) gap: Roman dredging in ancient Mediterranean harbours. Bollettino di Archeologia 1, 23–32.
Müller, C., Woelz, S., Ersoy, Y., Boyce, J., Jokisch, T., Wendt, G., Rabbel, W., 2009. Ultra-high-resolution marine 2D–3D seismic investigation of the Liman Tepe/Karantina Island archaeological site (Urla/Turkey). J. Appl. Geophys. 68 (1), 124–134.
Öztürk, B., Dogan, A., Bakir, B.B., Salman, A., 2014. Marine molluscs of the Turkish coasts: an updated checklist. Turkish J. Zool. 38 (6), 832–879.
Papadopoulos, J.K., 2014. Greece in the Early Iron Age: mobility, commodities, polities, and literacy. In: Knapp, B.A., Van Dommelen, P. (Eds.), The Cambridge Prehistory of the Bronze and Iron Age Mediterranean. Cambridge University Press, pp. 178–195.
Pasqualini, V., Pergent-Martini, C., Clabaut, P., Pergent, G., 1998. Mapping of *Posidonia oceanica* using aerial photographs and side scan sonar: Application off the Island of Corsica (France). Estuar. Coast. Shelf Sci. 47 (3), 359–367.
Pint, A., Seeliger, M., Frenzel, P., Feuser, S., Erkul, E., Berndt, C., Klein, C., Pirson, F., Brückner, H., 2015. The environs of Elaia's ancient open harbour–a reconstruction based on microfaunal evidence. J. Archaeol. Sci. 54, 340–355.
Piva, A., Asioli, A., Schneider, R.R., Trincardi, F., Andersen, N., Colmenero-Hidalgo, E., Dennielou, B., Flores, J.-A., Vigliotti, L., 2008. Climatic cycles as expressed in sediments of the PROMESS1 borehole PRAD1-2, central Adriatic, for the last 370 ka: 1. Integrated stratigraphy. Geochem. Geophys. Geosyst. 9 (1).
Raban, A., 1995. Dor-Yam: maritime and coastal installations at Dor in their geomorphological and stratigraphic context. In: Excavations at Dor. Final report. Vol. 1., Areas A and C. Introduction and Stratigraphy, pp. 285–354.
Ramkumar, M., 2015. Toward Standardization of Terminologies and Recognition of Chemostratigraphy as a Formal Stratigraphic Method. Chemostratigraphy Elsevier, pp. 1–21.
Reimer, P.J., Reimer, R.W., 2001. A marine reservoir correction database and on-line interface. Radiocarbon 43 (2A), 461–463.
Reimer, R.W., Reimer, P.J., 2017. An online application for ΔR calculation. Radiocarbon 59 (5), 1623–1627.
Reimer, P.J., Austin, W.E., Bard, E., Bayliss, A., Blackwell, P.G., Ramsey, C.B., Butzin, M., Cheng, H., Edwards, R.L., Friedrich, M., Grootes, P.M., 2020. The IntCal20 Northern Hemisphere radiocarbon age calibration curve (0–55 cal kBP). Radiocarbon 62 (4), 725–757.
Riddick, N.L., Boyce, J.I., Reinhardt, E.G., Rothaus, R.M., Chomicki, K.M., McCarthy, F. M., 2021. Multi-proxy palaeoenvironmental record of coastal tectonic uplift and abandonment (ca. 6th c. CE) of Lechaion's inner harbour, ancient Corinth, Greece. Quat. Sci. Rev. 267, 107080 https://doi.org/10.1016/j.quascirev.2021.107293.
Riddick, N.L., Boyce, J.I., Krezoski, G.M., Şahoğlu, V., Erkanal, H., Tuğcu, I., Alkan, Y., Gabriel, J.J., Reinhardt, E.G., Goodman-Tchernov, B.N., 2022a. Palaeoshoreline reconstruction and underwater archaeological potential of Liman Tepe: a long-occupied coastal prehistoric site in western Anatolia, Turkey. Quat. Sci. Rev. 276, 107293.
Riddick, N.L., Boyce, J.I., Sahoglu, V., Tuğcu, İ., Alkan, Y., Reinhardt, E.G., Goodman-Tchernov, B.N., 2022b. Datasets: Coastal palaeoenvironmental record of Late Bronze to Iron Age harbour development at Liman Tepe-Clazomenae, western Anatolia, Turkey. Mendeley Data V1. https://doi.org/10.17632/fbkv5dj64f.1.
Roberts, N., Allcock, S.L., Barnett, H., Mather, A., Eastwood, W.J., Jones, M., Primmer, N., Yiğitbaşıoğlu, H., Vannière, B., 2019. Cause-and-effect in Mediterranean erosion: the role of humans and climate upon Holocene sediment flux into a central Anatolian lake catchment. Geomorphology 331, 36–48.
Rothwell, R.G., Croudace, I.W., 2015. Micro-XRF studies of sediment cores: A perspective on capability and application in the environmental sciences. In: Croudace, I.W., Rothwell, R.G. (Eds.), Micro-XRF Studies of Sediment Cores. Springer, pp. 1–24.
Şahoğlu, V., 2005. The Anatolian trade network and the Izmir region during the Early bronze age. Oxf. J. Archaeol. 24 (4), 339–361.
Şahoğlu, V., 2010. Ankara University Research Center for Maritime Archaeology (ANKÜSAM) and its role in the Protection of Turkey's Underwater Cultural Heritage. In Congress.
Sayın, E., 2003. Physical features of the Izmir Bay. Cont. Shelf Res. 23 (10), 957–970.
Sayın, E., Eronat, C., 2018. The dynamics of İzmir Bay under the effects of wind and thermohaline forces. Ocean Sci. 14 (2), 285–292.
Scott, D.B., Hermelin, J.O.R., 1993. A device for precision splitting of micropaleontological samples in liquid suspension. J. Paleontol. 67 (1), 151–154.
Seki, A., Tada, R., Kurokawa, S., Murayama, M., 2019. High-resolution Quaternary record of marine organic carbon content in the hemipelagic sediments of the Japan Sea from bromine counts measured by XRF core scanner. Progr. Earth Planet. Sci. 6 (1), 1–12.
Shalev, A.E., Gilboa, A., Yasur-Landau, A., 2019. The Iron Age maritime interface at the south Bay of Tel Dor: results from the 2016 and 2017 excavation seasons. Int. J. Naut. Archaeol. 48 (2), 439–452.
Skrabal, S.A., Terry, C.M., 2002. Distributions of dissolved titanium in porewaters of estuarine and coastal marine sediments. Mar. Chem. 77 (2–3), 109–122.
Sonnenburg, E.P., Boyce, J.I., 2008. Data-fused digital bathymetry and side-scan sonar as a base for archaeological inventory of submerged landscapes in the Rideau Canal, Ontario, Canada. Geoarchaeology 23 (5), 654–674.
Stuiver, M., Reimer, P.J., Reimer, R.W., 2021. CALIB 8.2 [WWW program] at. http://calib.org.
Tartaron, T.F., 2013. Maritime Networks in the Mycenaean World. Cambridge University Press.
Tuğcu, İ., 2017. Investigation of the Liman Tepe/Klazomenai ancient harbour eastern breakwater. J. Cukurova Univ. Instit. Soc. Sci. 26 (1), 85–101.
Tuncel, R., Şahoğlu, V., 2018. The Chalcolithic of coastal western Anatolia: a view from Liman Tepe, Izmir. In: Dietz, S., Mavridis, F., Tabkosic, Z., Takaoglu, T. (Eds.), Communities in Transition: The Circum-Aegean Area during the 5th and 4th Millennia BC. Oxbow Books Limited.
Van Andel, T.H., Zangger, E., Demitrack, A., 1990. Land use and soil erosion in prehistoric and historical Greece. J. Field Archaeol. 17 (4), 379–396.
Votruba, G.F., Artzy, M., 2016. An Archaic anchor arm from Liman Tepe/Klazomenai, Turkey. Int. J. Naut. Archaeol. 45 (2), 450–456.
Wei, T., Simko, V., Levy, M., Xie, Y., Jin, Y., Zemla, J., 2017. Package 'corrplot'. Statistician 56 (316), e24.
Wolters, S., Zeiler, M., Bungenstock, F., 2010. Early Holocene environmental history of sunken landscapes: pollen, plant macrofossil and geochemical analyses from the Borkum Riffgrund, southern North Sea. Int. J. Earth Sci. 99 (8), 1707–1719.
Ziegler, M., Jilbert, T., de Lange, G.J., Lourens, L.J., Reichart, G.J., 2008. Bromine counts from XRF scanning as an estimate of the marine organic carbon content of sediment cores. Geochem. Geophys. Geosyst. 9 (5).